

UC Davis

UC Davis Previously Published Works

Title

Tropical mountain ice core $\delta^{18}O$: A Goldilocks indicator for global temperature change.

Permalink

<https://escholarship.org/uc/item/7xz3v8qg>

Journal

Science Advances, 9(45)

Authors

Liu, Zhengyu

Bao, Yuntao

Thompson, Lonnie

et al.

Publication Date

2023-11-10

DOI

10.1126/sciadv.adi6725

Peer reviewed

CLIMATOLOGY

Tropical mountain ice core $\delta^{18}\text{O}$: A Goldilocks indicator for global temperature changeZhengyu Liu^{1,2,3*}, Yuntao Bao^{1†}, Lonnie G. Thompson^{3,4}, Ellen Mosley-Thompson^{1,3}, Clay Tabor⁵, Guang J. Zhang⁶, Mi Yan², Marcus Lofverstrom⁷, Isabel Montanez⁸, Jessica Oster⁹

Very high tropical alpine ice cores provide a distinct paleoclimate record for climate changes in the middle and upper troposphere. However, the climatic interpretation of a key proxy, the stable water oxygen isotopic ratio in ice cores ($\delta^{18}\text{O}_{\text{ice}}$), remains an outstanding problem. Here, combining proxy records with climate models, modern satellite measurements, and radiative-convective equilibrium theory, we show that the tropical $\delta^{18}\text{O}_{\text{ice}}$ is an indicator of the temperature of the middle and upper troposphere, with a glacial cooling of $-7.35^\circ \pm 1.1^\circ\text{C}$ (66% CI). Moreover, it severs as a “Goldilocks-type” indicator of global mean surface temperature change, providing the first estimate of glacial stage cooling that is independent of marine proxies as $-5.9^\circ \pm 1.2^\circ\text{C}$. Combined with all estimations available gives the maximum likelihood estimate of glacial cooling as $-5.85^\circ \pm 0.51^\circ\text{C}$.

INTRODUCTION

The tropical mountain ice core stable water isotope ratio ($\delta^{18}\text{O}_{\text{ice}}$) provides a distinct paleoclimate proxy in the mid- to upper troposphere, in contrast to lowlands $\delta^{18}\text{O}$ records that reflect near sea level climate changes. However, even after four decades of study (1–8), the climatic interpretation of tropical $\delta^{18}\text{O}_{\text{ice}}$ has remained highly controversial. At high latitudes, polar ice core $\delta^{18}\text{O}_{\text{ice}}$ has been established as a proxy for temperature via the Rayleigh distillation process in the so called “temperature effect” (9–12). In the tropics, most studies have focused on cave speleothem $\delta^{18}\text{O}$ in the lowlands and suggest it as a proxy for precipitation via hydrological processes (13–20) due to the “amount effect” (9, 21). However, neither interpretation above appears to apply directly to tropical $\delta^{18}\text{O}_{\text{ice}}$. In previous studies, tropical $\delta^{18}\text{O}_{\text{ice}}$ has been interpreted as a proxy for either temperature (3, 4, 22) or precipitation with important contribution from remote convective moisture sources from Amazon basin (22–35). These conflicting results have led to the long outstanding question: Is tropical $\delta^{18}\text{O}_{\text{ice}}$ a proxy for temperature or precipitation? Here, combining paleo $\delta^{18}\text{O}_{\text{ice}}$ records with climate models, modern remote sensing measurements of vapor $\delta^{18}\text{O}_v$, and a radiative-convective equilibrium theory, we show that tropical $\delta^{18}\text{O}_{\text{ice}}$ represents the temperature change in the tropical mid- to upper troposphere for deglacial climate change, caused mainly by Rayleigh distillation and thermodynamic processes. Furthermore, in contrast to all other temperature records, which only reflect regional changes, the tropical ice core record provides a “Goldilocks” indicator of global mean surface temperature

(GMST) change during the deglaciation, providing the first estimate of glacial GMST cooling independent of oceanic proxies.

RESULTS AND DISCUSSION

Model-data comparison of precipitation $\delta^{18}\text{O}$ over the last deglaciation

We first examine the classical Huascarán $\delta^{18}\text{O}_{\text{ice}}$ in comparison with a transient simulation of climate-isotope coevolution over the last deglaciation [20 to 11 thousand years (ka); Fig. 1] [iTRACE, Materials and Methods, and fig. S1, (18)]. Observational $\delta^{18}\text{O}_{\text{ice}}$ is dominated by an enrichment trend of about 6.5 per mil (‰) during the last deglaciation, with two modest depletion periods during Heinrich Stadial 1 (~18 to 15 ka) and the Younger Dryas (~13 to 12 ka) that bracket an enrichment during the Bølling-Allerød warming (~14.5 to 13 ka) (Fig. 1D, gray) (3). The iTRACE precipitation $\delta^{18}\text{O}_p$ over Huascarán, however, exhibits a completely different evolution profile that is dominated by millennial variability with an amplitude of only 2‰ (Fig. 1D, green). This $\delta^{18}\text{O}_p$ variability is negatively correlated with the millennial variability of local precipitation, in the sense of isotopic “amount effect” (Fig. 1D, blue), similar to previous modeling studies on other time periods (22, 27, 32–34). The discrepancy of the model $\delta^{18}\text{O}_p$ from observational $\delta^{18}\text{O}_{\text{ice}}$ seems unlikely to be caused by sublimation in the ice cores. Instead, as shown below, this model-data inconsistency quite likely results from one serious model deficiency in the study of tropical Andes (22, 32, 36, 37): the model topography. Because of the limited model resolution, model topography at the Huascarán ice core grid is only 830 m in iTRACE, much lower than the 6050-m elevation in the real world (Fig. 1, E and G).

Model $\delta^{18}\text{O}$ change with elevation

It remains technically challenging to directly compare model $\delta^{18}\text{O}_p$ with ice core $\delta^{18}\text{O}_{\text{ice}}$ at the ice core elevation, because the resolution of global climate models cannot resolve isolated high mountain peaks. We propose an alternative approach, which is to treat the change of model vapor $\delta^{18}\text{O}_v(z)$ as an approximation of $\delta^{18}\text{O}_p$ at the altitude z as if the mountain did peak at z in the model.

¹Department of Geography, Ohio State University, Columbus, OH, USA. ²School of Geography Science, Nanjing Normal University, Nanjing, China. ³Byrd Polar and Climate Research Center, Ohio State University, Columbus, OH, USA. ⁴School of Earth Sciences, Ohio State University, Columbus, OH, USA. ⁵Department of Earth Sciences, University of Connecticut, Storrs, CT, USA. ⁶Scripps Institute of Oceanography, University of California, San Diego, San Diego, CA, USA. ⁷Department of Geosciences, University of Arizona, Tucson, AZ, USA. ⁸Department of Earth and Planetary Sciences, University of California–Davis, Davis, CA, USA. ⁹Department of Earth and Environmental Sciences, Vanderbilt University, Nashville, TN, USA.

*Corresponding author. Email: liu.7022@osu.edu

†These authors contributed equally to this work.

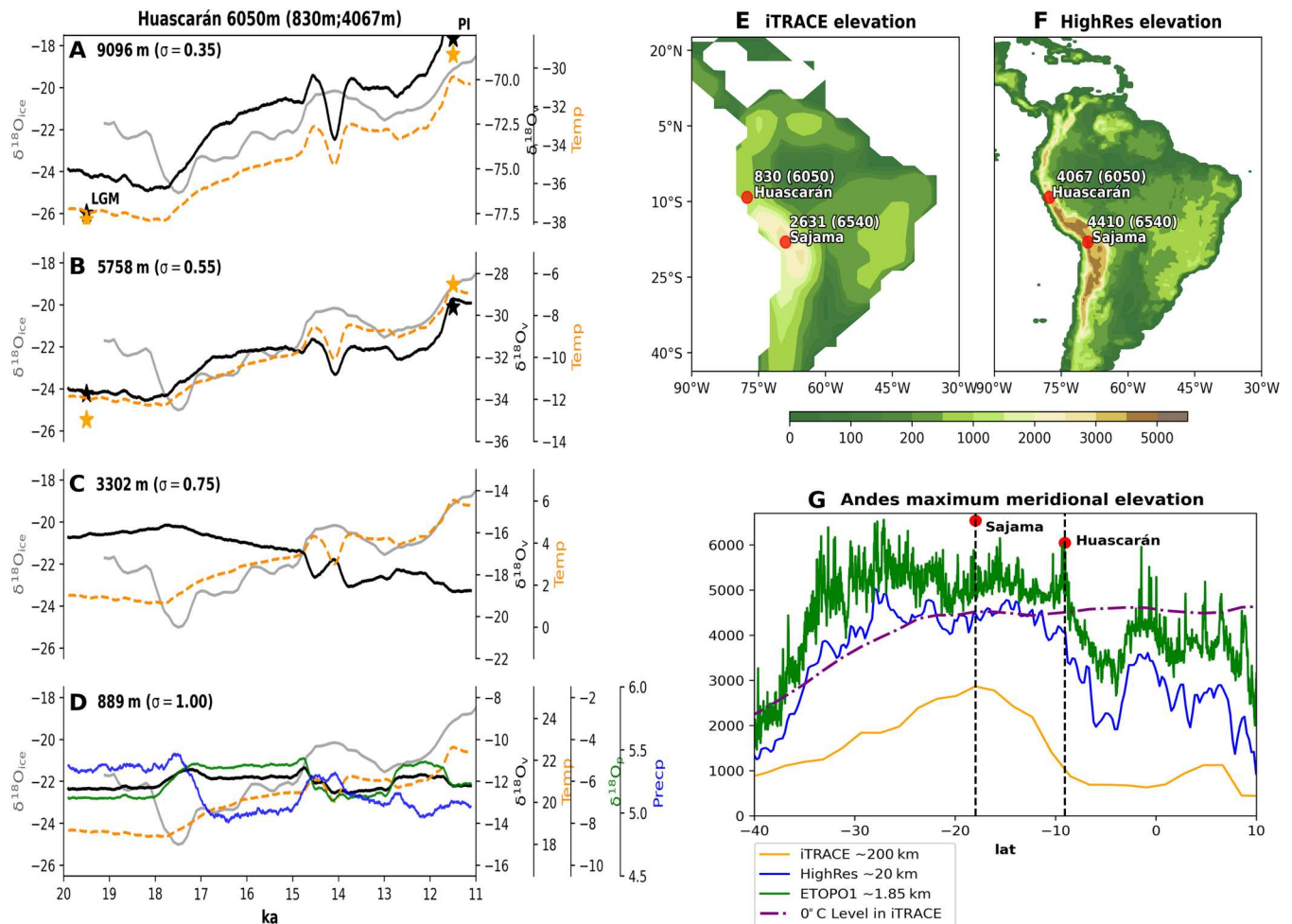


Fig. 1. Model-data comparison for the last deglaciation on Huascarán. Time series of ice core $\delta^{18}\text{O}_{\text{ice}}$ (gray, in ‰) in (A to D) Huascarán compared with iTRACE model (200-year running mean) vapor $\delta^{18}\text{O}_v$ (black, in ‰) and temperature (orange, in °C) at different altitude (σ level), and, in addition, precipitation (blue, in mm/day) and precipitation $\delta^{18}\text{O}_p$ (green, in ‰) at the surface (D). Also shown in (A) and (B) are the $\delta^{18}\text{O}_v$ (black star) and temperature (orange star) in the HighRes iCAM model at LGM and preindustrial (PI), marked at 19.5 and 11.5 ka, respectively, with the $\delta^{18}\text{O}_v$ offset by 6.5, 4‰ in (A) and (B), respectively. Model topography (in m) is shown for (E) iTRACE and (F) HighRes over South America, with the elevations of Huascarán and Sajama marked for the model (real world). The highest topography along the Andes is shown in (G) for iTRACE (orange) and HighRes (blue), and the real world (green), with the real-world Huascarán and Sajama marked in red and the annual freezing level in iTRACE PI (purple). It is seen that $\delta^{18}\text{O}_v$ changes markedly with height, while temperature change remains similar with height, such that at high elevations, $\delta^{18}\text{O}_v$ variability resembles temperature.

Hence, the $\delta^{18}\text{O}_{\text{ice}}$ record will be compared with the model $\delta^{18}\text{O}_v(z)$ of the altitude of the ice core site. Despite the potential difference between $\delta^{18}\text{O}_p$ and $\delta^{18}\text{O}_v$, associated with condensation and mixing processes, their changes over long climate time scales are likely to be similar because $\delta^{18}\text{O}_p$ depends critically on the environment $\delta^{18}\text{O}_v$, aside from about a 7‰ enrichment due to condensation fractionation and mixing (38). This similarity is seen in the deglacial evolution of $\delta^{18}\text{O}_p$ and the near surface $\delta^{18}\text{O}_v$ at Huascarán in iTRACE (Fig. 1D, black versus green), and, more generally, in the high correlation between $\delta^{18}\text{O}_p$ and near surface $\delta^{18}\text{O}_v$ (more precisely, weighted by precipitation as $\delta^{18}\text{O}_{vp}$) in iTRACE over the globe (fig. S2).

The deglacial evolution of $\delta^{18}\text{O}_v(z)$ in iTRACE changes markedly with elevation at Huascarán, from a weak isotopic depletion trend in the lower atmosphere (below 3000 m; Fig. 1C, black) to a strong enrichment trend in the middle and upper troposphere (above 5000

m) (Fig. 1, A and B, black). The evolution of model $\delta^{18}\text{O}_v$ at the ice core elevation closely resembles that of the observed $\delta^{18}\text{O}_{\text{ice}}$, except for about 6‰ enrichment of $\delta^{18}\text{O}_{\text{ice}}$ as expected from the condensation fractionation and mixing processes (Fig. 1B). Temperature exhibits a warming trend with increasing amplitude from the surface to the upper troposphere (orange, Fig. 1, A to D) such that the evolution of $\delta^{18}\text{O}_v(z)$ at and above the ice core site closely resembles that of temperature. This vertical change of $\delta^{18}\text{O}_v$ variability leads to a reversal of the correlation between $\delta^{18}\text{O}_v$ and temperature $\text{cor} <\delta^{18}\text{O}_v, T>$ from negative to positive from the lower to upper troposphere. This vertical change of $\delta^{18}\text{O}_v$ variability is confirmed to be robust in a pair of high-resolution atmospheric model simulations for the Last Glacial Maximum (LGM) and preindustrial period (PI) (HighRes, 25 km resolution, Materials and Methods), as seen in the $\delta^{18}\text{O}_v$ and temperature (Fig. 1, marked at 19 ka for LGM and 11.5 ka for PI in black stars

and orange dots, respectively). A largely similar vertical change of $\delta^{18}\text{O}_v$ can also be seen in Sajama, another Andean ice core on the tropical margin (4) (fig. S3 and text S1).

The correlation sign reversal with elevation is a general phenomenon over the entire tropics as shown globally in the zonal mean of $\text{cor} \langle \delta^{18}\text{O}_v, T \rangle$ with height and latitude (Fig. 2A). In the tropics, the correlation reverses from negative to positive with height systematically, such that $\text{cor} \langle \delta^{18}\text{O}_v, T \rangle$ is positive in the upper troposphere, consistent with the sense of isotopic “temperature effect” there. This correlation structure is largely zonally uniform such that $\delta^{18}\text{O}_v$ variability over the Andes is representative of the tropics overall (text S2 and figs. S4 and S5). Furthermore, the positive correlation observed throughout almost all the upper tropical troposphere extends

toward both poles via the middle and lower troposphere. Thus, the upper tropical troposphere appears like the “third pole” for $\delta^{18}\text{O}_v$, which is dominated by the temperature effect as in the other two poles. Last, this extensive positive correlation “layer” aloft is separated from the lower atmosphere by a zero correlation level that coincides roughly with the annual freezing level (the green dash dot line in Fig. 2A).

The positive global paleothermometer slope $d\delta^{18}\text{O}_v/dT$ derived from the $\delta^{18}\text{O}_v - T$ regression in the upper tropical troposphere is mainly determined by the cooling trend (instead of millennial variability) from PI (0 ka) to LGM (20 ka), as seen in the similar $d\delta^{18}\text{O}_v/dT$ calculated from the difference between the two snapshots of LGM and PI (fig. S6C). This cooling trend is caused by a

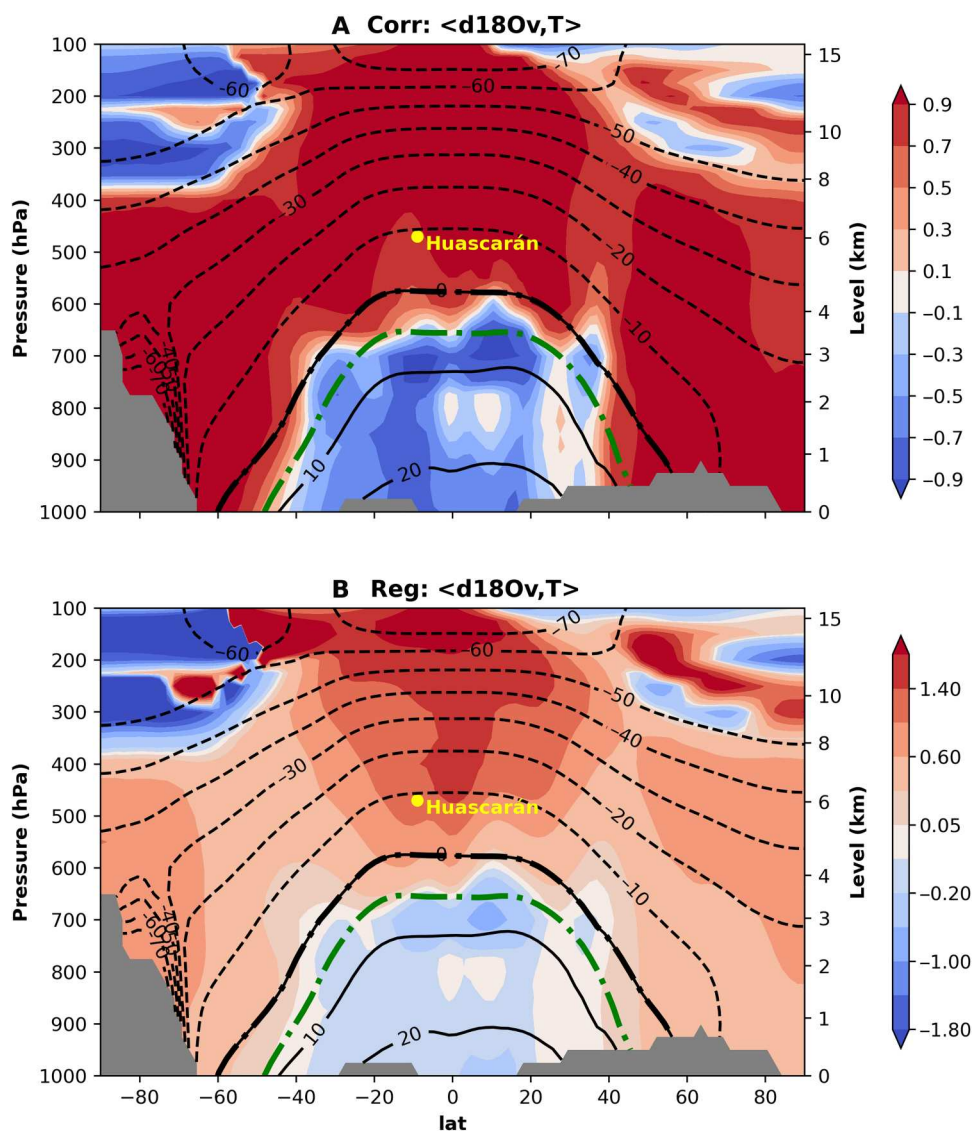


Fig. 2. Global vapor $\delta^{18}\text{O}_v$ and temperature relation during deglaciation. Zonal mean of (A) temporal correlation (after 500-year running mean) between the $\delta^{18}\text{O}_v$ (‰) and the temperature ($^{\circ}\text{C}$) at the same location (longitude, latitude, and altitude) and (B) $d\delta^{18}\text{O}_v/dT$ regression slope (‰/ $^{\circ}\text{C}$) from 21 to 11 ka in iTRACE (shading). Zonal mean climatology temperatures at the PI are also plotted in each panel (black contours). The annual freezing level (0 $^{\circ}\text{C}$) is plotted in heavy black and green dash dot line for PI and LGM, respectively. Real-world Huascarán is also marked. Since temperature cools at the LGM relative to the PI, precipitation decreases in the tropics at the LGM relative to the PI. Thus, a negative $\delta^{18}\text{O}_v$ correlation (or slope) with temperature is in the sense as the amount effect, and a positive correlation indicates the dominance of temperature effect.

global cooling throughout the atmospheric column, but a vertical reversal of $\delta^{18}\text{O}_v$ change in the tropics (fig. S6a). A similar response of $\delta^{18}\text{O}_v$ and temperature between LGM and PI and the resulting $d\delta^{18}\text{O}_v/dT$ slope can also be seen along the Andes (fig. S7, A and C). This deglacial response in iTRACE is also robust in the HighRes model, as seen in the LGM-PI difference in $\delta^{18}\text{O}_v$, temperature and the $d\delta^{18}\text{O}_v/dT$ slope in global zonal mean (fig. S6, B and D) and along the north-south section of Andes (fig. S7, B and D). Note that, even in the HighRes, model topography at Huascarán (4067 m) is still below the annual freezing level, while the ice core site is well above the freezing level (Fig. 1, F and G, and fig. S7, B and D). A further analysis of three sensitivity experiments accompanying iTRACE (Materials and Methods) suggests that the reversal of $\text{cor} <\delta^{18}\text{O}_v, T>$ is robust in response to individual forcings [greenhouse gases (GHG), ice sheet, meltwater, and orbital forcing] as seen in the correlation and the regression slope $d\delta^{18}\text{O}_v/dT$ (fig. S8).

The positive $\text{cor} <\delta^{18}\text{O}_v, T>$ in the upper troposphere that reflects the temperature effect is accompanied by a negative $\text{cor} <\delta^{18}\text{O}_v, T>$ in the lower tropical atmosphere. This negative $\text{cor} <\delta^{18}\text{O}_v, T>$ is in the same sign as the amount effect response to deglacial warming as in previous modeling (18, 20) and observational (40, 41) studies of cave speleothem $\delta^{18}\text{O}_c$ and partly by the direct melting water effect of sea water $\delta^{18}\text{O}_{sw}$ change (fig. S9 and text S3) (42). Thus, our models suggest that the climate impact on $\delta^{18}\text{O}$ in the tropics strongly depends on the altitude, dominated by the response in the sense of amount effect in the lower atmosphere as observed in lowland cave speleothem records but also by the response in the sense of temperature effect in the upper troposphere as reflected in polar ice cores.

Reversal of the $\delta^{18}\text{O}$ response in satellite observations

The reversal of water isotope variability with height is confirmed in modern observations of interannual variability in two independent satellite measurements of vapor HDO/H₂O: tropospheric emission spectrometer (TES) (43, 44) and MUSICA (Multiplatform remote Sensing of Isotopologs for investigating the Cycle of Atmospheric water) IASI (Infrared Atmospheric Sounding Interferometer) (Materials and Methods) (45). The vertical change in δD_v variability, which could be inferred from its different responses to El Niño and Southern Oscillation between the surface and 500 hPa in TES (46), is confirmed in our systematic analysis of TES and IASI across pressure levels and in our models (fig. S10 and text S4). This vertical change in δD_v interannual variability is demonstrated more clearly in the vertical profile of correlation between monthly TES $\delta D_v(z)$ at different levels and the surface $\delta D_v(0)$ for each point in the tropics. The vertical profiles of $\text{cor} <\delta D_v(z), \delta D_v(0)>$ in the tropics change predominantly from positive at the surface to negative above 700 hPa (Fig. 3A). Independently, the sign reversal of $\delta^{18}\text{O}_v$ variability can also be seen in the mid-troposphere IASI δD_v correlated with the precipitation δD_p over the GNIP (Global Network of Isotopes in Precipitation) stations in the tropical Pacific and Atlantic region (Materials and Methods) (Fig. 3E). The surface δD_p correlation with local precipitation and surface temperature are negative (stars and triangles in Fig. 3E), consistent with the amount effect at these stations. These features of the correlations on interannual variability are also found consistent in iTRACE and HighRes models (Fig. 3, B, C, F, and G). The consistent vertical structure of interannual isotope variability between our

models and two independent satellite measurements provides strong support for the vertical reversal of the isotope response in our models for deglacial variability in iTRACE, which has been discussed earlier in Fig. 2 and, similarly to the interannual variability, in the vertical profiles of the correlation of deglacial variability in Fig. 3 (D and H).

Mechanism for the reversal of the $\delta^{18}\text{O}$ response

The sign reversal of tropical $\delta^{18}\text{O}_v$ variability is caused fundamentally by atmospheric thermodynamics and Rayleigh distillation process, with further contribution from convection-induced mixing. In a radiative convective equilibrium (RCE) theory of a coupled water vapor/isotope system that consists of a saturated cloud plume embedded in a broad environment (47, 48), the vertical depletion slope of the environmental $\delta^{18}\text{O}_v$, i.e. the isotopic lapse rate, can be derived as

$$|\partial_z(\delta^{18}\text{O}_v)| \approx N |\partial_z(\delta^{18}\text{O}_v)_{\text{Rayleigh}}| \quad (1)$$

where $N > 0$ is a non-Rayleigh factor that depends on mixing processes, and $|\partial_z(\delta^{18}\text{O}_v)_{\text{Rayleigh}}|$ is the isotopic lapse rate of the Rayleigh process that depends predominantly on the environmental temperature T and lapse rate Γ as (Materials and Methods)

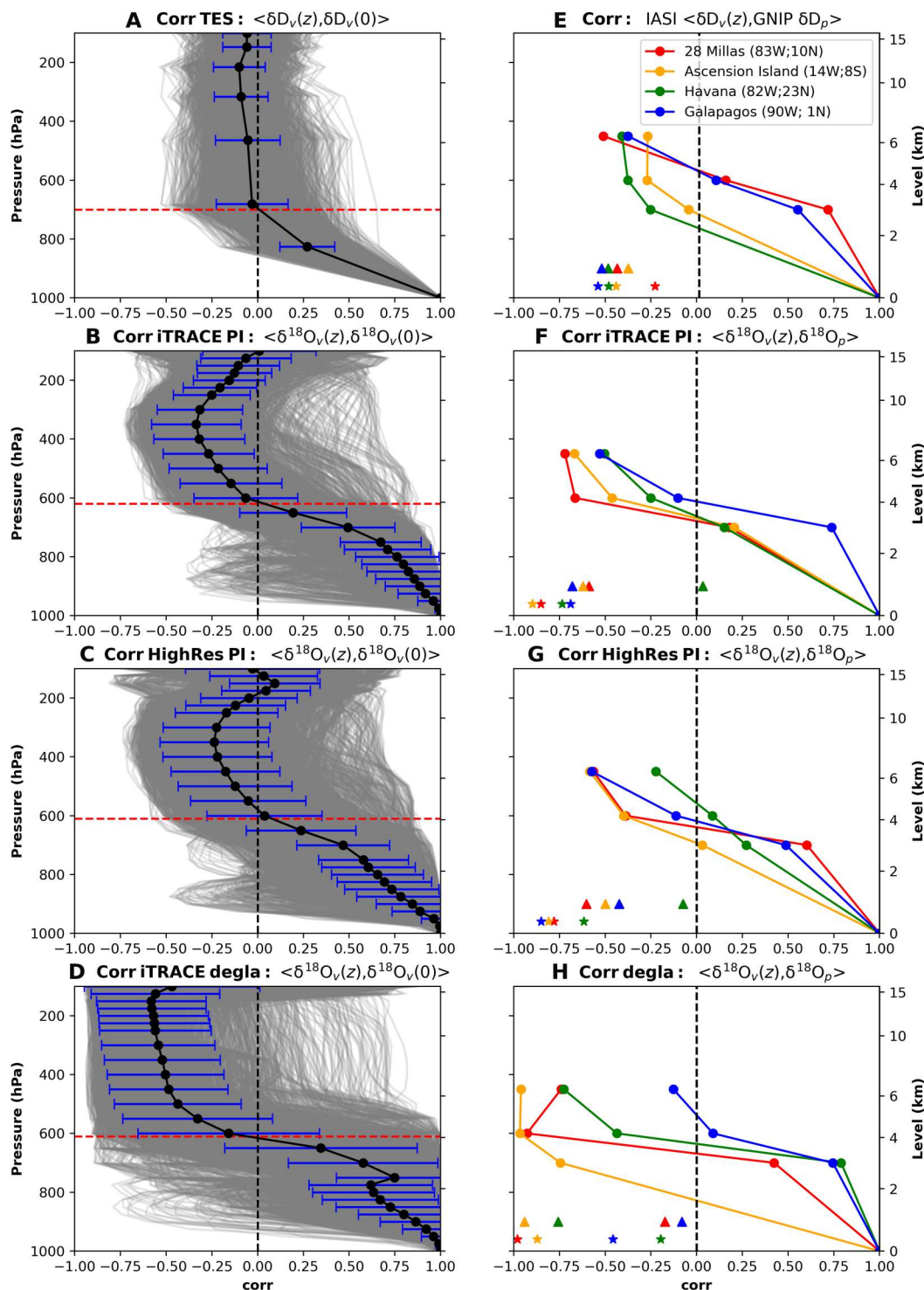
$$|\partial_z(\delta^{18}\text{O}_v)_{\text{Rayleigh}}| \sim \Gamma/T^2 \quad (2)$$

This Rayleigh solution suggests that a colder temperature and a larger temperature lapse rate (as in LGM cooling) lead to a steeper isotopic depletion slope in the environment $\delta^{18}\text{O}_v$. This is one key factor that causes the reversal of $\delta^{18}\text{O}_v$ response with elevation. Furthermore, convective mixing may further enhance the isotopic lapse rate to $N > 1$, by enriching the upper troposphere through detrainment (49) and depleting the lower atmosphere through rain re-evaporation (50), unsaturated downdraft at low rainfall rates, and equilibration with subcloud vapor at high rainfall rates (Materials and Methods) (49).

Here, we take the LGM-PI cooling as an example. Near the surface, the $\delta^{18}\text{O}_v$ is increased at LGM relative to PI by two effects. The first is the reduced precipitation associated with the amount effect, which is caused by various processes in deep convection systems (9), including the change of condensation altitude, the re-evaporation of large size of droplets and its diffusive exchange with the surrounding vapor and the recycling of the subcloud layer vapor feeding the convective system (21, 39, 51). The second is the increase of sea water isotope that is caused by the trapping of light isotopes over continental ice sheets (text S3). Upward in the mid- to upper troposphere, however, the $\delta^{18}\text{O}_v$ response is eventually reversed to decrease because the colder temperature at LGM leads to a stronger decrease of $\delta^{18}\text{O}_v$ with elevation at LGM than PI, as shown in Eqs. 1 and 2 (fig. S11, A and B, and Materials and Methods). Furthermore, the magnitude of the reversed $\delta^{18}\text{O}_v$ response in the tropics in iTRACE can be diagnosed quantitatively using the theoretical solution of our RCE model or Rayleigh distillation model, along with the iTRACE model temperature (figs. S11, C to F, S12, S13, and S14, and Materials and Methods), further supporting the dominant role of Rayleigh distillation process, enhanced by convective mixing, in producing the temperature effect of $\delta^{18}\text{O}_v$ in the mid- to upper troposphere.

Last, the temperature effect of $\delta^{18}\text{O}_v$ in the mid- to upper troposphere is determined predominantly by the response of the isotopic

Fig. 3. Vertical structure of isotope variability. (A) Temporal correlation between monthly vapor [$\delta D_v(z)$] at each data level and that at the surface 1000 hPa [$\delta D_v(0)$] in TES observation over tropics (20°S–20°N). (B) Same as (A) but for $\delta^{18}O_v$ in iTRACE PI simulation at each model level. (C) Same as (B) but for HighRes PI simulation. (D) Same as in (B) for iTRACE, but for 500-year running mean variability for the deglacial evolution in 21 to 11 ka. Gray lines are for the correlation profiles at all available grid points, the heavy black line for the ensemble mean of all points, blue ticks for a 1- σ ensemble spread, and the red dashed line for the reversal level of ensemble mean correlation. For visualization, the HighRes are calculated after binning the data onto a $2^\circ \times 2^\circ$ box before correlation. (E) Temporal correlation between IASI monthly vapor $\delta D_v(z)$ at three data levels and precipitation δD_p (dots with connected lines) over four GNIP stations in the eastern equatorial Pacific-Atlantic region (surface value 1 as δD_p correlation with itself). Also marked near the surface are the correlations between GNIP δD_p and precipitation (stars) and surface temperature (triangles). (F) Same as (E) but for $\delta^{18}O_v$ in iTRACE PI simulation. (G) Same as (E) but for HighRes PI simulation. (H) Same as in (F) for iTRACE, but for 500-year running mean variability for the deglacial evolution in 21 to 11 ka.



lapse rate with temperature as shown in Eqs. 1 and 2, instead of the surface $\delta^{18}O_v$ response and/or the reversal. This follows because the magnitude of $\delta^{18}O_v$ change is usually much smaller near the surface than in the upper troposphere. Thus, a colder (warmer) atmospheric column will always lead to a steeper (flatters) isotopic lapse rate $|\partial_z \delta^{18}O_v|$ and, in turn, a depleted (enriched) $\delta^{18}O_v$ response in the mid- to upper troposphere, regardless of the sign of the small $\delta^{18}O_v$,

response near the surface. Therefore, the temperature effect of $\delta^{18}O_v$ in the upper troposphere is determined robustly by Rayleigh distillation and thermodynamic processes. The near-surface response of $\delta^{18}O_v$ (and $\delta^{18}O_p$), however, is determined by more complex processes associated with the amount effect, and, in addition, by the change of sea water $\delta^{18}O_{sw}$ during deglaciation (text S3 and Materials and Methods). The reversal response discussed above,

however, reconciles the seemingly conflicting results between the amount effect in low-elevation $\delta^{18}\text{O}_p$ and the temperature effect of high-elevation $\delta^{18}\text{O}_{\text{ice}}$ in the tropics.

Tropical temperature change

Our model LGM-PI cooling is about -7°C at the Huascarán site (fig. S7, A and C). This cooling agrees with the lower end estimation of -8°C from Thompson *et al.* (3) based on the present day spatial slope $\Delta\delta^{18}\text{O}_p/\Delta T \approx 1\text{‰}/^\circ\text{C}$ in Antarctica, because this spatial slope happens to be close to our model deglacial temporal slope $\Delta\delta^{18}\text{O}_v/\Delta T \approx 1\text{‰}/^\circ\text{C}$ at the Huascarán site (figs. S7, B and D, S15, and text S5). This cooling over the Andes is a good representation of the overall tropical cooling at the same altitude in models (fig. S6, A and C), as expected from the weak horizontal temperature gradient response in the tropical free atmosphere (52). At the surface, our model temperature in the tropics cools by -4°C over the ocean and by -5°C over land (fig. S16, A and B). The stronger cooling over lowlands is consistent with paleo reconstructions (53–56). The 4°C sea surface temperature (SST) cooling of model SST, while greater than the -2° to -3°C cooling in most SST reconstructions so far (57), is consistent with a recent data assimilation reanalysis (58, 59). Overall, the annual freezing level in the tropics is lowered by 960 m (from 4.63 to 3.67 km; figs. S12 and S16C), consistent with the 900-m lowering of snowline deduced from observations (55). Unlike the weaker SST cooling that is found to be inconsistent with the snowline and ice core data in observations (23, 24, 53, 60), our -4°C surface cooling is dynamically consistent with the stronger alpine cooling in our models, mainly in response to reduced CO_2 (61). Thus, Huascarán $\delta^{18}\text{O}_{\text{ice}}$ acted as a “weather station tower” that continuously recorded the history of tropical temperature change in the mid- to upper troposphere, along with low-level changes recorded in other proxies.

A Goldilocks indicator of global temperature change

In contrast to other known temperature records, which tend to represent regional temperature changes, the tropical mid-troposphere is unique in that its temperature is also an excellent indicator of GMST change during deglaciation, both qualitatively and quantitatively. Qualitatively, the deglacial temperature evolution is similar between the GMST and the tropics throughout the atmospheric column in iTRACE (fig. S17, A and B). This occurs because the tropics are located in the proximity of the nodal point of the inter-hemispheric bipolar seesaw temperature response associated with the millennial variability of the Atlantic Meridional Overturning Circulation. Hence, millennial temperature variability is greatly suppressed in both the global mean and the tropics. This leaves a deglacial temperature evolution dominated by a warming trend that is forced by the rising CO_2 and retreating ice sheet in iTRACE (fig. S17, C to E), as in the reconstructed GMST (Fig. 4A) (59, 62). This representation of mid-troposphere temperature also explains the overall consistency among ice core $\delta^{18}\text{O}$ records in different parts of the tropics in the observation (63).

This temperature variability in the tropical mid-troposphere further serves as a Goldilocks indicator of the GMST variability, quantitatively. This is evident in the nearly identical magnitude of deglacial evolution between the Huascarán temperature and GMST in iTRACE (Fig. 4A). Physically, the magnitude of the atmospheric temperature response increases upward in low latitudes along with the response of the moisture lapse rate (61) but increases downward

at high latitudes due to strong stability and the surface albedo feedback (fig. S6, A and B). The opposite vertical temperature responses between low and high latitudes compensate to produce nearly the same magnitude of glacial cooling below the mid-troposphere for the global mean temperature in iTRACE, and, robustly, across a wide range of climate models (fig. S18). Hence, the tropical mid-troposphere is ubiquitously at the Goldilocks spot where the deglacial temperature variability is quantitatively the closest to that of GMST, as shown as the minimum deviation of deglacial temperature change from GMST in iTRACE (Fig. 4B). This vertical structure of temperature response in iTRACE is robust across climate models in the LGM-PI difference across HighRes and Paleoclimate Model Intercomparison Project (64, 65) (PMIP) models (figs. S18 and S19 and text S6).

First solely land proxy-based estimation of GMST glacial cooling

For the best estimation of GMST, we convert the Huascarán $\delta^{18}\text{O}_{\text{ice}}$ to ΔGMST using the ensemble of models available along with some minor adjustments related to, say, the sea level change (Materials and Methods). First, the Huascarán temperature is reconstructed from the Huascarán $\delta^{18}\text{O}_{\text{ice}}$ using the Huascarán temporal slope derived from the HighRes model $\Delta\delta^{18}\text{O}_v/\Delta T = 0.88 \pm 0.13\text{‰}/^\circ\text{C}$ (1σ) (Fig. 5A). This gives the mid-troposphere cooling $\Delta T_{\text{Huascarán}} = -7.35^\circ \pm 0.11^\circ\text{C}$ based on the LGM-PI isotope difference $\Delta\delta^{18}\text{O}_{\text{ice}} = -6.5\text{‰}$. Next, the ΔGMST is reconstructed from this $\Delta T_{\text{Huascarán}}$ using the Goldilocks’ scaling factor $\Delta\text{GMST}/\Delta T_{\text{Huascarán}} = 0.80 \pm 0.11$ that is derived from the grand ensemble of PIMP and iCESM models (Fig. 5A). The deglacial evolution of our reconstructed ΔGMST is in overall good agreement with the latest reconstruction from the LGM Reanalysis (LGMR) (44), especially given the chronology uncertainty of our $\delta^{18}\text{O}_{\text{ice}}$ record in the early period towards the LGM. For the LGM, there are nine quantitative estimations available with the medium ranging from -3° to -6.3°C (58, 66–74). Our Huascarán-derived LGM cooling is $\Delta\text{GMST} = -5.9^\circ \pm 1.2^\circ\text{C}$, with six of nine previous medium estimations within our 66% confidence level (Fig. 5B). Our estimation is the only land-based estimation independent of marine proxies, while all previous estimations can be considered based on marine proxies because they rely solely (58, 67, 68, 71–73) or mostly (66, 69, 70, 74) on marine proxies, which have various potential errors (58, 72). Furthermore, in contrast to all surface temperature proxies, which tend to represent local temperature changes and therefore require dense network to reconstruct GMST, our $\delta^{18}\text{O}_{\text{ice}}$ record is unique in its Goldilocks position high up in the tropical atmosphere column such that it can represent global temperature change by itself. Last, given all the estimates and their uncertainties, we have the maximum likelihood estimation of the LGM cooling as $\Delta\text{GMST}_{\text{Optimal}} = -5.85^\circ \pm 0.51^\circ\text{C}$ (Materials and Methods), suggesting the high-end LGM cooling and climate sensitivity.

MATERIALS AND METHODS

Method 1: Models: The iTRACE simulation

The iTRACE is performed in the state-of-the-art iCESM1.3 with water isotopes enabled (66) from 20,000 to 11,000 years ago (20 to 11 ka) under realistic external forcing of GHG, orbital, ice sheet, and ocean bathymetry as well as meltwater forcing (18). The iCESM1.3 is composed of the community atmosphere model

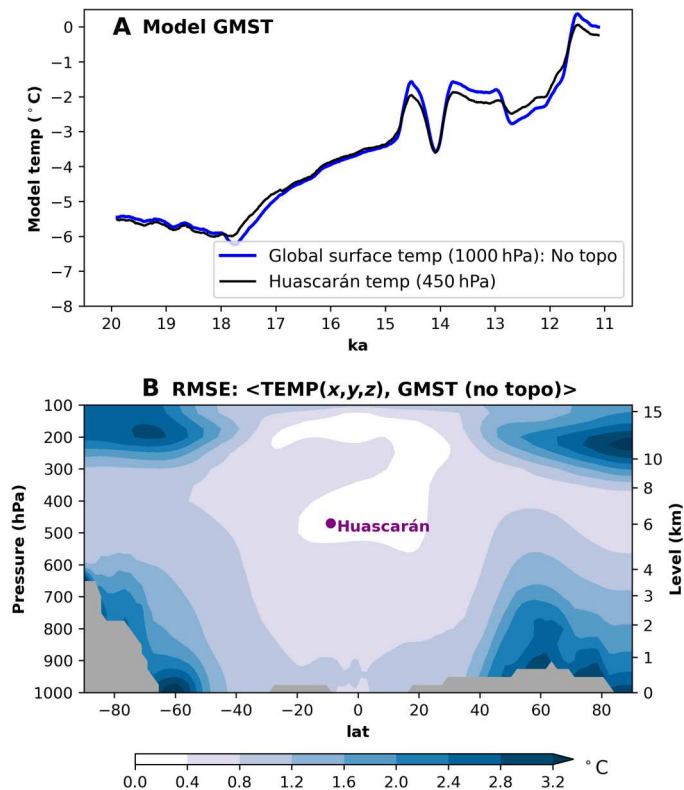


Fig. 4. Huascarán and global temperature evolution in iTRACE. (A) Deglacial annual temperature (°C) for Huascarán and GMST. (B) Zonal mean of the root mean square deviation of iTRACE deglacial temperature variability at each grid point from the GMST variability (°C). Huascarán temperature variability exhibits the GMST variability quantitatively, because of its Goldilocks location in the tropical mid-atmosphere where temperature variability exhibits minimum deviation from the GMST variability.

(CAM5.3), Parallel Ocean Program, version 2 (POP2), Los Alamos Sea Ice Model, version 4 (CICE4), and Community Land Model, version 4 (CLM4). The resolution of atmosphere and land is nominal 2° resolutions (1.9° in latitude and 2.5° in longitude), with 30 vertical levels in the atmosphere; the resolution of ocean and sea ice is nominal 1° horizontal resolutions (gx1v6), with 60 vertical levels in the ocean. Our iCESM1.3 reproduces the present-day climate reasonably well, similar to CESM1.2, iTRACE reproduces well the deglacial evolution of water isotope observed in the Asian monsoon region and polar regions (18, 75, 76). The iTRACE experiment is performed along with three forcing sensitivity experiments with the forcing factors added one by one, first the ice sheet (ICE-6G), then the orbital forcing, and last GHG, forming three transient sensitivity experiments, ICE, ICE + ORB, and ICE + ORB + GHG, respectively. The baseline iTRACE simulation (also, ICE + ORB + GHG + MWF) is branched off from the ICE + ORB + GHG run at 19 ka, with the meltwater forcing imposed. These experiments allow us to estimate the impact of each forcing effect approximately as: ice sheet (experiment ICE), orbital (experiment ICE + ORB – experiment ICE), GHG (experiment ICE + ORB + GHG – experiment ICE + ORB), meltwater flux (experiment iTRACE – experiment ICE + ORB + GHG).

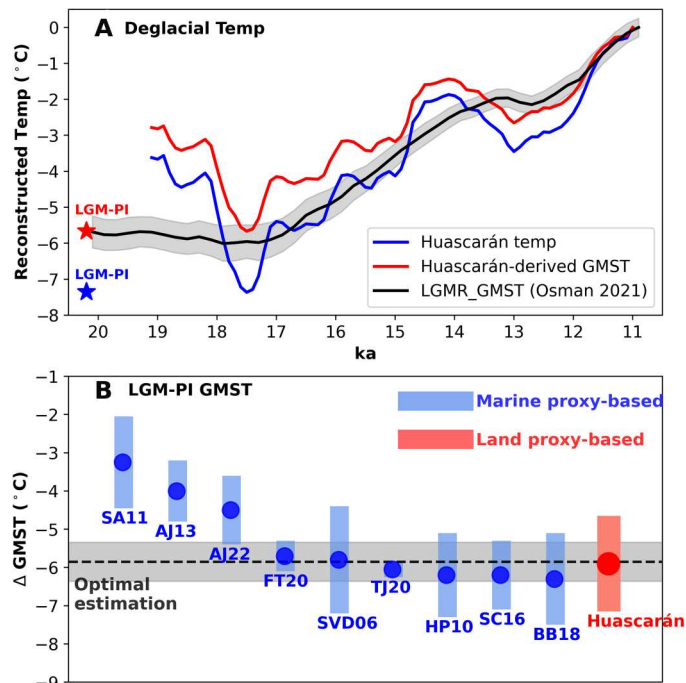


Fig. 5. Reconstruction of Huascarán temperature and GMST. (A) Deglacial temperature (°C) at Huascarán (blue) and for GMST (red) reconstructed from the Huascarán $\delta^{18}O_{ice}$ record (3) along with the GMST reconstruction from the LGMR (44) (black, shading 95% level). The blue and red stars represent the LGM-PI difference for Huascarán and GMST. (B) Estimates of LGM cooling Δ GMST from previous studies [blue bars, including SA11 (53), AJ13 (54), AJ22 (58), FT20 (57), SVD06 (51), TJ20 (43), HP10 (52), SC16 (55), and BB18 (56)] and our Huascarán $\delta^{18}O_{ice}$ reconstruction (red bars), respectively. Dots show the median, vertical bars represent the 66% CI, as derived from the original publications. Previous estimations are based on marine proxies, either solely or predominantly, while our estimation is based on a Goldilocks land-record only. The blackline represents the maximum likelihood estimation derived from all the 10 estimations, with the gray shading for the 66% CI.

The HighRes simulations are two snapshot experiments of the atmospheric component model of iCESM1.3 forced by 25 years of monthly SST and sea ice cover created using LGM (21 ka) and PI simulations branched off from iTRACE. Here, the atmosphere and land components are active and use iCAM5.3 and iCLM4, respectively. The HighRes simulations have roughly 25 km horizontal resolution (0.23° in latitude and 0.31° in longitude) and 30 vertical levels in the atmosphere.

In both models, the native vertical coordinate for the atmosphere is in the hybrid σ -pressure coordinate, with $\sigma = 1$ and 0 at the surface and top of atmosphere, respectively. Most analyses are performed here on the processed data interpolated onto the pressure level.

Method 2: iTRACE, climatology comparison with GNIP around the Andes

The global distribution of iTRACE model climatology of climate and isotopes of the present day has been validated against observations (66), and its seasonal cycles are compared with GNIP observations (<https://iaea.org/services/networks/gnip>) for the Asian region (18) and lowlands of the South America monsoon region (19). Here, we further compare the model climatology of both

iTRACE model and HighRes against GNIP observations in two stations over the Andes: Marcapomacocha (76.3°W, 11.4°S) (fig. S1, A1 to C1) and Laica (68.1°W, 16.5°S) (fig. S1, A2 to C2). It is seen that the model seasonal cycle of temperature, precipitation and $\delta^{18}\text{O}_p$ compare well with GNIP observation, except for larger amplitude of precipitation in the model, possibly due to the warm SST bias along the tropical eastern Pacific and low topography due to coarse model resolution (not shown). The low topography in the iTRACE model also produced a warm bias.

Method 3: Present satellite observations and analyses

To study the vertical structure of interannual variability of stable water isotopes, we analyze vapor δD_v from the paired measurements of HDO/H₂O in two independent satellite data sets. The first set is the TES (43, 44), which is available for the period of 2004 to 2012 on five tropospheric levels (316, 454, 681, 825, and 1000 hPa). The second set is MUSICA IASI (45) (level 3 product regridded to a regular $1^\circ \times 1^\circ$ grid; <https://essd.copernicus.org/articles/13/5273/2021/#section5>), which is available for the period of 2014 to 2020 on three tropospheric levels (454, 600, and 700 hPa). Since IASI does not have surface data, we use as a substitute for the precipitation δD_p over GNIP stations from 2012 to 2017 under the Coordinated Research Project F31004 sponsored by the International Atomic Energy Agency. Figure 3 (E to H) shows the vertical structure of the temporal correlation $\langle \delta D_v, \delta D_p \rangle$ during the overlapping period of δD_v (IASI) and δD_p over four GNIP stations around the tropical East Pacific and tropical Atlantic region: Galapagos, Ecuador (90.3°W, 0.74°N), Havana, Cuba (82.22°W, 23°N), 28 Millas, Costa Rica (83.37°W, 10.1°N), and Ascension Island, Saint Helena (14.2°W, 7.92°S). The correlation is also made between δD_p and station surface temperature and precipitation (as markers around the 900 hPa level). Several points are worth noting. First, in Fig. 3 and fig. S10, the interannual correlations are calculated using the total monthly data. The signs of the correlations remain similar if the correlations are made separately for the seasonal cycle and the monthly anomaly after removing the seasonal cycle. This is consistent with our RCE theory (later in method 4) that the sign reversal is caused by the rapid local convective process. Second, the model correlations are virtually the same for both δD and $\delta^{18}\text{O}$. Third, the sign reversal of the vertical profiles of $\text{cor} \langle \delta^{18}\text{O}_v(z), \delta^{18}\text{O}_v(0) \rangle$ in Fig. 3 (A to D) becomes even clearer if we confine the correlation in the subregions of strong convection and heavy precipitation, say, annual mean rainfall greater than 4 mm/day. This is consistent with the convective mechanism discussed in the RCE model (later in method 4). It has been pointed out that the surface data in TES are less certain (44, 46). This may explain the weaker negative correlation $\text{cor} \langle \delta^{18}\text{O}_v(z), \delta^{18}\text{O}_v(0) \rangle$ in the mid-troposphere in TES, which is only about -0.2 in TES (Fig. 3A), but reaches about -0.5 in IASI (Fig. 3E) and the models (Fig. 3, B, C, F, and G).

Method 4: RCE theory for isotope response with elevation

We use a simple bulk-plume model under the RCE assumption, in which the convective cloud and the environment are treated as two "bulk plumes," each of homogenous properties at altitude z , with the cloud occupying a negligible fraction of area (47). In addition, a heavy isotope (H_2^{18}O or HDO) is also incorporated along with the light water isotope or water vapor (H_2^{16}O) (48). To focus on the isotope, here, we used the temperature and, in turn, lapse rate,

as given. The basic equations and solutions have been studied in detail by Romps (47) and Duan *et al.* (48), and are presented briefly here for the readers' convenience. The coupled moisture-isotope system consists of five equations for the vertical fluxes in the column of the free atmosphere

$$d_z M = \varepsilon M - \delta M \quad (3a)$$

$$d_z (Mq_c) = \varepsilon Mq_v - \delta Mq_c - c \quad (3b)$$

$$d_z (-Mq_e) = -\varepsilon Mq_e + \delta Mq_c + \xi c(z + \Delta z) \quad (3c)$$

$$d_z (Mq'_c) = \varepsilon Mq'_e - \delta Mq'_c - \alpha \frac{q'_c}{q_c} c \quad (3d)$$

$$d_z (-Mq'_e) = -\varepsilon Mq'_e + \delta Mq'_c + \xi \alpha \frac{q'_c(z + \Delta z)}{q_c(z + \Delta z)} c(z + \Delta z) \quad (3e)$$

Equation 3a is for the total ascent mass flux M in the cloud plume (with units of $\text{kg m}^{-2} \text{s}^{-1}$), which is accompanied by an equal amount of decent mass flux $-M$ in the environment. Equations 3b and 3c are the moisture budget in the clouds and environment, respectively, with q_c and q_v as the mass mixing ratio of ordinary moisture H_2^{16}O (or specific humidity) in clouds and environment, respectively, and, furthermore, q_c being assumed in saturation. Parallel to the two moisture equations, Eqs. 3d and 3e are for the heavy isotopes in cloud and environment, respectively, with q'_c and q'_v being the mass ratios of heavy isotopes H_2O^{18} in clouds and environment, respectively. The fractional rates of entrainment and detrainment of moisture are ε and δ , respectively, which are related to each other for a given vertical profile of mass flux $M(z)$ due to mass conservation. The c is the condensation rate, from which a proportion of ξ evaporates while falling over a distance of Δz , such that the precipitation efficiency is $1 - \xi$. The $\alpha \approx 1.015$ is the fractionation coefficient for oxygen water isotopes in the mid- to upper troposphere because the original equations for HDO are now adapted for H_2O^{18} .

Following Duan *et al.* (48), we assume equal fractional entrainment and detrainment rates $\delta = \varepsilon$, which are justified because of the overall comparable magnitudes of entrainment and detrainment fluxes in the free atmosphere in vertical average (77). Since, in general, the relative humidity of the environmental air, $\text{RH} = q_v/q_c$, varies slowly with height, one can derive from Eqs. 3a to 3c an analytical solution [in the Wentzel-Kramers-Brillouin (WKB) approximation (78)] of an exponential vertical profile of water vapor (47)

$$q_c(z) = q_c(0)e^{-\gamma z}, q_v(z) = \text{RH}q_c(0)e^{-\gamma z} \quad (4a)$$

where $q_c(0)$ is the specific humidity at the base of the cloud or free atmosphere, or the lifting condensation level, and

$$c = [\gamma - \varepsilon(1 - \text{RH})]Mq_c, \text{RH} = \frac{\varepsilon + a\xi\gamma - a\xi\varepsilon}{\varepsilon + \gamma - a\xi\varepsilon} \quad (4b)$$

where $a = e^{-\gamma\Delta z}$. The water-vapor lapse rate can be approximated by

using the Clausius-Clapeyron relationship as (47)

$$\gamma = \frac{L\Gamma}{R_v T^2} - \frac{g}{R_a T} \approx \frac{L\Gamma}{R_v T^2} \quad (5)$$

where the first term that is associated with the saturation water vapor pressure dominates over the second term that is associated with air pressure. Here, $L = 2.45 \times 10^6 \text{ J kg}^{-1}$, $R_v = 461 \text{ J kg}^{-1}\text{K}^{-1}$, $R_a = 287 \text{ J kg}^{-1}\text{K}^{-1}$, and $g = 9.8 \text{ ms}^{-2}$ are fundamental constants of the latent heat of evaporation, specific gas constants of water vapor and dry air, and gravitational acceleration. The Γ and T are the temperature lapse rate and air temperature of the environment. In theory, they are constants evaluated at the base of cloud (47). Consistent with the WKB approximation (78) of the solution in Eqs. 4a and 4b, nevertheless, Γ and T can also be evaluated approximately locally at each altitude, as done for our model diagnosis in fig. S11 (C to F). In the application for diagnosing iTRACE in figs. S11 (C to F) and S12, the nonconstant Γ and T cause the vertical profile to deviate substantially from the purely exponential solution in the idealized case in fig. S11 (A and B).

Analogous to the water-vapor solution, the isotope can also be solved in a WBK solution in the exponential form as

$$q'_c(z) = q'_c(0)e^{-\gamma'z}, q'_v(z) = \text{RH}' q'_c(0)e^{-\gamma'z} \quad (6)$$

where $\text{RH}' = q'_v/q'_c$ is the heavy isotope relative humidity in the environment relative to that in the cloud, and γ' is the heavy isotope vapor lapse rate in the cloud. Given the solution for water vapor of c , RH in Eqs. 3a to 3e, the corresponding isotope solutions of γ' and RH' can also be derived from Eqs. 3d and 3e to satisfy the equations

$$\gamma'^2 - \alpha \frac{\gamma^2}{\varepsilon + \gamma - a\xi\varepsilon} \gamma' - (1 - b\xi)\alpha\varepsilon \frac{\gamma^2}{\varepsilon + \gamma - a\xi\varepsilon} = 0 \quad (7)$$

and

$$\text{RH}' = 1 - \frac{1}{\gamma'} (1 - b\xi)\alpha \frac{\gamma^2}{\varepsilon + \gamma - a\xi\varepsilon} \quad (8)$$

Here, $b = e^{-\gamma'\Delta z} = a^{\gamma'/\gamma}$, such that Eq. 7 is an implicit equation that can be solved numerically through root finding, except in the case of $\Delta z = 0$, where Eq. 7 reduces to a quadratic equation for γ' and can be solved analytically. The final solution for the vertical isotope profile in the cloud and environment can be derived in general as (48)

$$\delta^{18}\text{O}_c(z) = [1 + \delta^{18}\text{O}_c(0)]e^{-(\gamma'-\gamma)z} - 1 \quad (9a)$$

$$\delta^{18}\text{O}_v(z) = \frac{\text{RH}'}{\text{RH}} [1 + \delta^{18}\text{O}_c(0)]e^{-(\gamma'-\gamma)z} - 1 \quad (9b)$$

To gain insight into the mechanism for the response of $\delta^{18}\text{O}(z)$ to climate change, here, we further derive an explicit solution by taking advantage of the small deviation of the fractionation coefficient from 1, i.e., $0 < \alpha - 1 \ll 1$. From Eqs. 4a and 4b and 6 to 8, the leading order perturbation solutions can be derived (on the small parameter $\alpha - 1$) as

$$\frac{\gamma'}{\gamma} - 1 \approx N(\varepsilon_\gamma, a, \xi)(\alpha - 1) \quad (10a)$$

where

$$N(\varepsilon_\gamma, a, \xi) = \frac{1 + \varepsilon_\gamma - a\xi\varepsilon_\gamma}{1 + 2(\varepsilon_\gamma - a\xi\varepsilon_\gamma) + \varepsilon_\gamma\xi a \ln(a)} \quad (10b)$$

$$\varepsilon_\gamma = \varepsilon/\gamma \quad (10c)$$

and

$$-\left(\frac{\text{RH}'}{\text{RH}} - 1\right) \approx \Delta(\varepsilon_\gamma, a, \xi)(\alpha - 1) \quad (11a)$$

where

$$\Delta(\varepsilon_\gamma, a, \xi) = \frac{\varepsilon_\gamma(1 - \xi a)^2 - \xi a \ln(a)}{\xi a + \varepsilon_\gamma(1 - \xi a)[1 + 2\xi a + 2\varepsilon_\gamma(1 - \xi a) + \xi a(\xi a + \varepsilon_\gamma)\ln(a)]} \quad (11b)$$

Thus, the vertical profile of isotopes in Eqs. 9a and 9b can be expressed at the leading order as

$$\delta^{18}\text{O}_c(z) \approx [1 + \delta^{18}\text{O}_c(0)]e^{-N(\alpha-1)\gamma z} - 1 \quad (12a)$$

$$\delta^{18}\text{O}_v(z) \approx [1 - \Delta(\alpha - 1)][1 + \delta^{18}\text{O}_c(0)]e^{-N(\alpha-1)\gamma z} - 1 \quad (12b)$$

One can further prove that $\Delta_\gamma > 0$ and $\Delta_R > 0$ for physically realistic ranges of parameters. Therefore, in general, we have

$$\gamma' > \gamma \quad (13)$$

and

$$\text{RH}' < \text{RH} \quad (14)$$

Equation 13 shows that, in general, the isotope lapse rate exceeds the water-vapor lapse rate $\gamma' > \gamma$ with fractionation ($\alpha > 1$), such that $\delta^{18}\text{O}_v(z)$ decreases with altitude. The asymptotic solution of Eqs. 10a and 11a is an excellent approximation of the full WKB solution solved numerically from Eq. 7. This can be seen in an example that compares the factor N derived from the numerical solution with the asymptotic solution (fig. S13, A versus B).

The key equation of our theory can be derived from Eq. 12b, or equivalently from Eqs. 9b and 10a to 10c for the isotope lapse rate

$$|\partial_z(\delta^{18}\text{O}_v)| = \gamma' - \gamma \approx N(\alpha - 1)\gamma \sim N(\alpha - 1)\Gamma/T^2 \quad (15)$$

where we have used Eq. 5 as $\gamma \sim \Gamma/T^2$. This equation states that the vertical profile of isotope in vapor $\delta^{18}\text{O}_v(z)$ steepens in response to a global cooling. This occurs because a global cooling of a decreased temperature T leads to an increased moisture lapse rate γ and, in turn, an increased isotopic lapse rate $\partial_z(\delta^{18}\text{O}_v)$ in $N(\alpha - 1)\gamma$. This steeper slope is a key for understanding the temperature effect of $\delta^{18}\text{O}_v$ in the upper troposphere, as well as the sign reversal of isotope response with height. Physically, this steeper lapse rate for a cooler climate is robust because it is determined fundamentally by the thermodynamics of Clausius-Clapeyron relationship (as seen in Eq. 5) and the Rayleigh distillation in the RCE model, instead of the mixing parameters. In the absence of entrainment/detrainment mixing ($\varepsilon = 0$), we have from Eq. 10b that $N = 1$, and, in turn, from Eq. 15

$$|\partial_z(\delta^{18}\text{O}_v)_{\text{Rayleigh}}| = (\alpha - 1)\gamma \quad (16)$$

This solution is labeled in "Rayleigh" because it is the isotopic lapse rate derived from the Rayleigh distillation relation (9, 79)

$$\delta^{18}\text{O}_v - \delta^{18}\text{O}_{v0} = (\alpha - 1)\ln(q/q_0) \quad (17)$$

if α is assumed a constant. With the saturation specific humidity $q = q_s(T)$ (as in the saturated cloud vapor q_c in Eq. 4a) and the corresponding moisture lapse rate in Eqs. 5 and 16 can be recovered immediately by the vertical differentiation of the Rayleigh relation (Eq. 17).

In our RCE model, the non-Rayleigh processes associated with mixing ($\varepsilon > 0$) and additionally re-evaporation ($\xi > 0$) play two roles. First, mixing modifies the isotope lapse rate in the cloud and, in turn, the environment (79). Combining the Rayleigh solution of Eq. 16 with the general isotope lapse rate Eq. 15 gives

$$\partial_z(\delta^{18}\text{O}_v) \approx N\partial_z(\delta^{18}\text{O}_v)_{\text{Rayleigh}} \quad (18)$$

Therefore, N is effectively the non-Rayleigh factor, which is determined by mixing and re-evaporation parameters as shown in Eq. 10. In the numerical solution of Eq. 6, an increase of mixing ε , or a decrease of reevaporation ξ , reduces the factor N , and, in turn, the isotope lapse rate, but only modestly. This can be seen in the factor N as a function of ε and ξ (in the case of $\Delta z = 0$ km; fig. S13, A and B). It is also seen that N is not very sensitive to the mixing parameters. For a reasonably realistic regime of either $\varepsilon < 0.3/\text{km}$, or $\xi > 0.5$ (47), N ranges from about 0.8 to 1. Second, one obvious role of the mixing process is the generation of environment vapor for both water-vapor and heavy isotope. Otherwise, the environment air would have been void of moisture and heavy isotopes with $\text{RH} = \text{RH}' = 0$, as seen by setting $\varepsilon = \xi = 0$ in Eqs. 4b and 11. This can also be seen in the example in fig. S13 (C and D).

We now discuss the theoretical RCE solution and its application. First, we show an idealized case with $\varepsilon = 0.2/\text{km}$ and $\xi = 0.65$, along with $\alpha = 1.015$, largely consistent with those diagnosed from the iTRACE PI simulation and previous works (47, 48). In this case, the factor $N = 0.85$, as seen in fig. S13 (A or B), and therefore, isotopic lapse rate is close to the Rayleigh distillation process of $N = 1$. Our solution offers an interpretation of the vertical reversal of $\delta^{18}\text{O}_v$ response, for example, for the case of LGM cooling as follows. We start with an idealized case of a constant temperature lapse rate ($\Gamma = 6.4^\circ\text{K}/\text{km}$ of moisture lapse rate in the tropics, e.g., fig. S12, B and E) such that the $\delta^{18}\text{O}_v(z)$ profile decreases exponentially as shown in Eq. 12b. Assume a cooling of the cloud-base temperature from 289°K at "PI" to 284°K at "LGM" ($\Delta T = -5^\circ\text{K}$). The near sea level isotopic enrichment is prescribed in the subcloud layer $\delta^{18}\text{O}_c(0)$ from -14‰ at PI to a slight enrichment of -13.4‰ at LGM as in iTRACE. The surface $\delta^{18}\text{O}_c(0)$ is prescribed here, as it results from two mechanisms that are not included in our RCE model: The amount effect, which is associated with complex processes such as downdraft re-entrainment and re-evaporation (21, 39, 51, 79), and the isotope change of sea water $\Delta\delta^{18}\text{O}_{sw}$ (text S3). The $\delta^{18}\text{O}_v(z)$ in our solution isotopically depletes exponentially with altitude for both LGM and PI (fig. S11A). Since the LGM depletion profile is slightly steeper than that for the PI due to the colder temperature, the $\delta^{18}\text{O}_v$ difference of LGM-PI ($\Delta\delta^{18}\text{O}_v$) shows an almost linear trend with altitude, reversing from the isotopic enrichment ($\Delta\delta^{18}\text{O}_v > 0$) near the surface to isotopic depletion ($\Delta\delta^{18}\text{O}_v < 0$) in the upper troposphere (above $z = 4.5$ km, or 600 hPa, in this case) (fig. S11B). The corresponding $\delta^{18}\text{O}_v - T$ regression slope

therefore changes from $\Delta\delta^{18}\text{O}_v/\Delta T < 0$ below to the temperature effect of $\Delta\delta^{18}\text{O}_v/\Delta T > 0$ aloft.

Our RCE theory can be applied successfully to diagnose the iTRACE response quantitatively, further supporting its interpretation of the temperature effect in the mid- to upper troposphere and the reversal. In iTRACE, the vertical profiles of $\delta^{18}\text{O}_v(z)$ at LGM and PI show isotopic depletion with height over the tropics, and the LGM-PI difference $\Delta\delta^{18}\text{O}_v(z)$ also reverses from isotopic enrichment to depletion above 600 hPa (fig. S11, C and D, black), qualitatively consistent with the idealized case in fig. S11 (A and B). Quantitatively, using the model vapor $\delta^{18}\text{O}_v$ at 900 hPa as $\delta^{18}\text{O}_c(0)$ (48), model temperature and the temperature lapse rate at each altitude as T and Γ , our theoretical RCE solution largely reproduces the vertical profiles of $\delta^{18}\text{O}_v(z)$ in the tropics for both LGM and PI, as well as the LGM-PI difference $\Delta\delta^{18}\text{O}_v(z)$, in good agreement with iTRACE (red in fig. S11, C and D). The $\delta^{18}\text{O}_v(z)$ isotopic lapse rate increases with height in iTRACE (fig. S12D), rather than being a constant as in the idealized case in fig. S11A because of the colder temperature T and increased lapse rate Γ with height in iTRACE (fig. S12, E and F), following Eq. 15. Hence, the response $\Delta\delta^{18}\text{O}_v(z)$ of LGM-PI changes from weakly positive in the lower atmosphere, to strongly negative above ~ 600 hPa (fig. S11D). Furthermore, our RCE solution can also be largely reproduced by the Rayleigh model (blue, fig. S11, C and D), suggesting the dominant role of Rayleigh distillation. The tropical isotope changes largely follow the Rayleigh process, as seen in the averaged vertical profiles of $\delta^{18}\text{O}_v(z)$ against specific humidity, temperature, and pressure (fig. S14, A to C). The Rayleigh profile shows clearly a steeper lapse rate with altitude (decreasing pressure in fig. S14C), which leads to a much depleted $\delta^{18}\text{O}_v$ in the mid- to upper tropics, reversing the weak enrichment at the sea level (1000 hPa). A similar diagnosis using the RCE model and Rayleigh model can also interpret the $\Delta\delta^{18}\text{O}_v(z)$ response over the Andes (with the subcloud layer chosen as 750 hPa; figs. S11, E and F, and S12, A to C).

Despite the dominant Rayleigh process, the isotope lapse rate can be enhanced by non-Rayleigh processes that are not included in our RCE model solution. Notably, a surface warming increases deep convection, which tends to enrich the upper troposphere through condensate detrainment and mixing (49, 79, 80), but depletes the lower troposphere by rain evaporation (21, 50, 79). The dominant detrainment (entrainment) in the upper (lower) troposphere tend therefore to increase the isotope lapse rate $|\partial_z(\delta^{18}\text{O}_v)|$, reinforcing the thermodynamic effect of Rayleigh process, effectively making the non-Rayleigh factor $N > 1$. This convective mixing effect, however, is not included in our RCE model solution, because our RCE solution assumes a constant and equal vertical profile of entrainment and detrainment rate $\delta = \varepsilon = \text{const}$ (48). In this case, an increase of entrainment and detrainment actually leads to a slight reduction of isotopic lapse rate, as seen in the solution of the factor N in fig. S13 (A or B). Nevertheless, this convective mixing effect is likely contributing to the response in our iCESM simulations. Figure S14D shows the vertical profiles of entrainment and detrainment averaged in the tropics in iTRACE. It shows clearly that the total detrainment is dominant in the mid- to upper troposphere (above 700 hPa), while the entrainment is dominant in the lower atmosphere, consistent with previous studies (81, 82). This entrainment/detrainment profile is consistent with having the convective mixing reinforcing the reversal response. The LGM-PI $\delta^{18}\text{O}_v$,

reversal response in iTRACE is stronger than those of both RCE model and Rayleigh model, with the former being more depleted (enriched) in the mid- to lower (upper) troposphere than the latter two (black versus red and blue in fig. S11, D and F). This excessive reversal response in iTRACE can, therefore, be explained by the convective mixing mechanism discussed above.

It should be noted that the interpretation of the Huascarán ice core using the theory and iTRACE model simulation assumes that the isotope lapse rate over Huascarán can be represented by that in the nearby environmental tropical atmosphere. This assumption is likely to be valid because Huascarán is a tall and isolate mountain peak, which could be treated virtually as a passive “weather tower” that does not disturb the environment atmospheric circulation and in turn the isotope lapse significantly. In some other regions of high plateaus, such as the Tibetan Plateau and the Altiplano, the large-scale topography can strongly disturb the atmospheric convection and the local isotope lapse rate, even leading to reversed isotopic lapse rate (83–85).

Method 5: Estimating LGM cooling

In all previous estimations, the ΔGMST was reconstructed from surface temperature proxies. Since surface temperature represents local changes, this approach requires a large network of datasets. Furthermore, since most of the surface temperature proxies are confined over oceans, all these previous estimations of ΔGMST rely either solely or mainly on SST proxies. Last, these SST proxies are converted to air temperature for GMST using climate models either directly using a scaling factor [e.g., (71)] or through model covariance between SST and surface air temperature [e.g. (58)]. Here, we reconstruct the ΔGMST from a single observation of Huascarán $\delta^{18}\text{O}_{\text{ice}}$, and multiple independent climate models. First, we convert the $\delta^{18}\text{O}_{\text{ice}}$ to the local temperature change $\Delta T_{\text{Huascarán}}$ using a deglacial temporal slope of $\Delta\delta^{18}\text{O}_{\text{ice}}/\Delta T_{\text{Huascarán}}$ and, then, the $\Delta T_{\text{Huascarán}}$ to ΔGMST using a Goldilocks scaling factor of $\Delta\text{GMST}/\Delta T_{\text{Huascarán}}$.

For the temporal slope, we use the precipitation-weighted vapor isotope $\Delta\delta^{18}\text{O}_{\text{vp}}$ and annual temperature $\Delta T_{\text{Huascarán}}$ in the HighRes simulations at the Huascarán grid point. The vapor $\delta^{18}\text{O}_{\text{v}}$ and temperature values are derived from an interpolation from neighboring levels to the height of 6050 m in the PI simulation and the 6170 m (=6050 m + 120 m) in the LGM simulation, with the 120-m adjustment for the sea level change. The precipitation weight is also adjusted with a bias correction that removes the difference of the precipitation seasonal cycle of the PI simulation from the observation at Marcapomacocha for PI and LGM (fig. S1B), although this bias correction only changes the $\Delta\delta^{18}\text{O}_{\text{vp}}$ slightly (fig. S1, blue versus black). This gives our best estimation of $\Delta\delta^{18}\text{O}_{\text{ice}}/\Delta T_{\text{Huascarán}} = \Delta\delta^{18}\text{O}_{\text{vp}}/\Delta T_{\text{Huascarán}} = 0.884 \text{‰/}^\circ\text{C}$. The reason we use HighRes (instead of iTRACE) is that it has a much higher horizontal resolution and model topography (25 km versus 200 km and 4067 m versus 830 m) and represents so far the best effort in the study of glacial isotope response over isolated mountain peaks. The uncertainty of this temporal slope, ideally, should be estimated from an ensemble of independent isotope-enabled model simulations of resolutions comparable with HighRes, which is however currently unavailable. Therefore, we adopt a crude estimation of the uncertainty of 15% of the slope (=0.884‰/°C × 15% = 0.13‰/°C) (1 σ) for several reasons. First, this uncertainty is related to the uncertainty between HighRes and iTRACE and the uncertainty of the spatial

changes within HighRes. The $\Delta\delta^{18}\text{O}_{\text{vp}}/\Delta T_{\text{Huascarán}}$ slope is 0.753‰/°C in iTRACE and 1.025‰/°C in HighRes (after being averaged first onto the iTRACE grid box). These three slopes therefore give about a 15% SD. Second, this 15% SD is comparable to the temperature Goldilocks scaling factor that is derived next across a mega-ensemble of 15 climate models. This spread has been attributed to the different parameterization of deep convection among these models (86, 87). Third, our iCESM seems unlikely to exhibit too large a bias in this temporal slope, because this model has been shown to reproduce the observed climate and isotopes of the present and past reasonably well (18–20, 66, 75, 76). Given the LGM-PI difference of $\Delta\delta^{18}\text{O}_{\text{ice}} = -6.5\text{‰}$ (3), this temporal slope gives the estimation of $\Delta T_{\text{Huascarán}} = 7.35 \pm 1.1^\circ\text{C}$.

For the Goldilocks scaling factor, we first calculate the ratio of LGM-PI temperature difference at the Huascarán site and for the GMST in each of the 15 grand-ensembles of climate models of PMIP2 (CCSM, ECHAM53-MPIO, FGOALS, HadCM3M2, and MIROC3.2), PIMP3 (CCSM4, GISS-E2-R, MRI-CGCM3, and MIROC-ESM), PMIP4 (AWI-ESM, MIROC-ES2L, and MPI-ESM), iTRACE, HighRes, and TRACE. An outlier IPSL model is not used, although it does not change the result substantially. This gives the scaling factor of $\Delta\text{GMST}/\Delta T_{\text{Huascarán}} = 0.803 \pm 0.11$ (1 σ). Again, a 120-m sea level adjustment has been made by increasing the LGM cooling by -0.816°C (using a lapse rate of $0.68^\circ\text{C}/100$ m) in each model before calculating the ratio. This gives the LGM cooling estimation of $\Delta\text{GMST} = -5.9 \pm 1.2^\circ\text{C}$, with our uncertainty including six of the previous nine medium estimations (Fig. 5B).

Last, note that, all the previous nine estimates are independent because they use different methods and climate models, even though they all rely heavily on the SST proxies. Thus, we have a total of 10 independent estimates of ΔGMST_i , along with their SDs σ_i (Fig. 5B). These can be combined to give the maximum likelihood estimation of the LGM cooling as

$$\Delta\text{GMST}_{\text{optimal}} = \frac{\sum_{i=1}^{10} \Delta\text{GMST}_i / \sigma_i^2}{\sum_{i=1}^{10} 1 / \sigma_i^2} = -5.8534^\circ\text{C}$$

with a reduced uncertainty as

$$\sigma = \frac{1}{\sqrt{\sum_{i=1}^{10} 1 / \sigma_i^2}} = 0.5087^\circ\text{C}$$

Again, this optimal cooling is very close to the medium of our Huascarán-derived estimate.

Supplementary Materials

This PDF file includes:

Texts S1 to S6
Figs. S1 to S19
References

REFERENCES AND NOTES

1. L. G. Thompson, Glaciological investigations of the tropical Quelccaya ice Cap, Peru. *J. Glaciol.* **25**, 69–84 (1980).

2. L. G. Thompson, E. Mosley-Thompson, B. M. Arno, El Niño-southern Oscillation events recorded in the stratigraphy of the tropical Quelccaya ice cap, Peru. *Science* **226**, 50–53 (1984).
3. L. G. Thompson, E. Mosley-Thompson, M. E. Davis, P.-N. Lin, K. A. Henderson, J. Cole-Dai, J. F. Bolzan, K.-B. Liu, Late glacial stage and Holocene tropical ice core records from Huascarán, Peru. *Science* **269**, 46–50 (1995).
4. L. G. Thompson, T. Yao, M. Davis, K. Henderson, E. Mosley-Thompson, P.-N. Lin, J. Beer, H.-A. Sval, J. Cole-Dai, J. Bolzan, Tropical climate instability: The last glacial cycle from a Qinghai-Tibetan ice core. *Science* **276**, 1821–1825 (1997).
5. L. G. Thompson, M. E. Davis, E. Mosley-Thompson, T. A. Sowers, K. A. Henderson, V. S. Zagorodnov, P.-N. Lin, V. N. Mikhalenko, R. K. Campen, J. F. Bolzan, A 25,000-year tropical climate history from Bolivian ice cores. *Science* **282**, 1858–1864 (1998).
6. L. G. Thompson, E. Mosley-Thompson, M. E. Davis, K. A. Henderson, H. H. Brecher, V. S. Zagorodnov, T. A. Mashiotta, P.-N. Lin, V. N. Mikhalenko, D. R. Hardy, J. Beer, Kilimanjaro ice core records: Evidence of Holocene climate change in tropical Africa. *Science* **298**, 589–593 (2002).
7. B. W. Bird, M. B. Abbott, M. Vuille, D. T. Rodbell, N. D. Stansell, M. F. Rosenmeier, A 2,300-year-long annually resolved record of the South American summer monsoon from the Peruvian Andes. *Proc. Natl. Acad. Sci. U.S.A.* **108**, 8583–8588 (2011).
8. M. Vuille, S. J. Burns, B. L. Taylor, F. W. Cruz, B. W. Bird, M. B. Abbott, L. C. Kanner, H. Cheng, V. F. Novello, A review of the South American monsoon history as recorded in stable isotopic proxies over the past two millennia. *Clim. Past* **8**, 1309–1321 (2012).
9. W. Dansgaard, Stable isotopes in precipitation. *Tellus* **16**, 436–468 (1964).
10. J. Jouzel, F. Vimeux, N. Caillon, G. Delage, G. Hoffmann, V. Masson-Delmotte, F. Parrenin, Magnitude of isotope/temperature scaling for interpretation of central Antarctic ice cores. *J. Geophys. Res. Atmos.* **108**, 10.1029/2002JD002677, (2003).
11. R. B. Alley, K. M. Cuffey, Oxygen- and hydrogen-isotopic ratios of water in precipitation: Beyond paleothermometry. *Rev. Mineral. Geochem.* **43**, 527–553 (2001).
12. K. Cuffey, W. S. B. Paterson, *“Ice Core Studies” in The physics of glaciers* (Academic Press, 2010), 645–647.
13. Y. J. Wang, H. Cheng, R. L. Edwards, Z. An, J. Y. Wu, C.-C. Shen, J. A. Dorale, A high-resolution absolute-dated late Pleistocene monsoon record from Hulu Cave, China. *Science* **294**, 2345–2348 (2001).
14. F. S. R. Pausata, D. S. Battisti, K. H. Nisancioglu, C. M. Bitz, Chinese stalagmite $\delta^{18}\text{O}$ controlled by changes in the Indian monsoon during a simulated Heinrich event. *Nat. Geosci.* **4**, 474–480 (2011).
15. Z. Liu, X. Wen, E. C. Brady, B. Otto-Bliesner, G. Yu, H. Lu, H. Cheng, Y. Wang, W. Zheng, Y. Ding, R. L. Edwards, J. Cheng, W. Liu, H. Yang, Chinese cave records and the East Asia summer monsoon. *Quat. Sci. Rev.* **83**, 115–128 (2014).
16. X. Liu, D. S. Battisti, The influence of orbital forcing of tropical insolation on the climate and isotopic composition of precipitation in South America. *J. Climate* **28**, 4841–4862 (2015).
17. J. C. H. Chiang, I. Y. Fung, C.-H. Wu, Y. Cai, J. P. Edman, Y. Liu, J. A. Day, T. Bhattacharya, Y. Mondal, C. A. Labrousse, Role of seasonal transitions and westerly jets in East Asian paleoclimate. *Quat. Sci. Rev.* **108**, 111–129 (2015).
18. C. He, Z. Liu, B. Otto-Bliesner, E. Brady, C. Zhu, R. Tomas, P. U. Clark, J. Zhu, A. Jahn, S. Gu, J. Zhang, J. Nusbaumer, D. Noone, Y. Wang, M. Yan, Y. Bao, Hydroclimate footprint of pan-Asian monsoon water isotope during the last deglaciation. *Sci. Adv.* **7**, eabe2611 (2021).
19. Y. Bao, Z. Liu, C. He, Dipole response of millennial variability in tropical South American precipitation and $\delta^{18}\text{O}_p$ during the last deglaciation: Part I: Rainfall response. *J. Climate* **36**, 4691–4707 (2023).
20. Y. Bao, Z. Liu, C. He, Dipole response of millennial variability in tropical South American precipitation and $\delta^{18}\text{O}_p$ during the last deglaciation: Part II: $\delta^{18}\text{O}_p$ response. *J. Climate* **36**, 4709–4721 (2023).
21. C. Risi, S. Bony, F. Vimeux, Influence of convective processes on the isotopic composition ($\delta^{18}\text{O}$ and δD) of precipitation and water vapor in the tropics: 2. Physical interpretation of the amount effect. *J. Geophys. Res. Atmos.* **113**, 10.1029/2008JD009943, (2008).
22. M. Vuille, R. S. Bradley, R. Healy, M. Werner, D. R. Hardy, L. G. Thompson, F. Keimig, Modeling $\delta^{18}\text{O}$ in precipitation over the tropical Americas: 2. Simulation of the stable isotope signal in Andean ice cores. *J. Geophys. Res. Atmos.* **108**, 10.1029/2001JD002039, (2003).
23. W. S. Broecker, Mountain glaciers: Recorders of atmospheric water vapor content? *Global Biogeochem. Cycles* **11**, 589–597 (1997).
24. R. T. Pierrehumbert, Huascarán $\delta^{18}\text{O}$ as an indicator of tropical climate during the Last Glacial Maximum. *Geophys. Res. Lett.* **26**, 1345–1348 (1999).
25. P. A. Baker, C. A. Rigby, G. O. Seltzer, S. C. Fritz, T. K. Lowenstein, N. P. Bacher, C. Veliz, Tropical climate changes at millennial and orbital timescales on the Bolivian Altiplano. *Nature* **409**, 698–701 (2001).
26. E. Ramirez, G. Hoffmann, J. D. Taupin, B. Francou, P. Ribstein, N. Caillon, F. Ferron, A. Landais, J. Petit, B. Pouyaud, U. Schotterer, J. C. Simoes, M. Stievenard, A new Andean deep ice core from Nevado Illimani (6350 m), Bolivia. *Earth Planet. Sci. Lett.* **212**, 337–350 (2003).
27. M. Vuille, M. Werner, Stable isotopes in precipitation recording South American summer monsoon and ENSO variability: Observations and model results. *Clim. Dynam.* **25**, 401–413 (2005).
28. K. E. Samuels-Crow, J. Galewsky, D. R. Hardy, Z. D. Sharp, J. Worden, C. Braun, Upwind convective influences on the isotopic composition of atmospheric water vapor over the tropical Andes. *J. Geophys. Res. Atmos.* **119**, 7051–7063 (2014).
29. P. G. Aron, C. J. Poulsen, R. P. Fiorella, N. E. Levin, R. P. Acosta, B. J. Yanites, E. J. Cassel, Variability and controls on $\delta^{18}\text{O}$, d-excess, and $\delta^{17}\text{O}$ in Southern Peruvian precipitation. *J. Geophys. Res. Atmos.* **126**, e2020JD034009 (2021).
30. R. P. Fiorella, C. J. Poulsen, R. S. Pillco Zola, J. B. Barnes, C. R. Tabor, T. A. Ehlers, Spatio-temporal variability of modern precipitation $\delta^{18}\text{O}$ in the central Andes and implications for paleoclimate and paleoaltimetry estimates. *J. Geophys. Res. Atmos.* **120**, 4630–4656 (2015).
31. H. Guy, A. Seimon, L. B. Perry, B. L. Konecky, M. Rado, M. Andrade, M. Potocki, P. A. Mayewski, Subseasonal variations of stable isotopes in tropical Andean precipitation. *J. Hydrometeorol.* **20**, 915–933 (2019).
32. N. Insel, C. J. Poulsen, C. Sturm, T. A. Ehlers, Climate controls on Andean precipitation $\delta^{18}\text{O}$ interannual variability. *J. Geophys. Res. Atmos.* **118**, 9721–9742 (2013).
33. F. Vimeux, R. Gallaire, S. Bony, G. Hoffmann, J. C. H. Chiang, What are the climate controls on δD in precipitation in the Zongo Valley (Bolivia)? Implications for the Illimani ice core interpretation. *Earth Planet. Sci. Lett.* **240**, 205–220 (2005).
34. F. Vimeux, G. Tremoy, C. Risi, R. Gallaire, A strong control of the South American SeeSaw on the intra-seasonal variability of the isotopic composition of precipitation in the Bolivian Andes. *Earth Planet. Sci. Lett.* **307**, 47–58 (2011).
35. L. R. Welp, E. J. Olson, A. L. Valdivia, J. R. Larico, E. P. Arhuire, L. M. Paredes, J. T. DeGraw, G. M. Michalski, Reinterpreting precipitation stable water isotope variability in the Andean Western Cordillera due to sub-seasonal moisture source changes and sub-cloud evaporation. *Geophys. Res. Lett.* **49**, e2022GL099876 (2022).
36. N. Insel, C. J. Poulsen, T. A. Ehlers, Influence of the Andes Mountains on South American moisture transport, convection, and precipitation. *Clim. Dynam.* **35**, 1477–1492 (2010).
37. C. J. Poulsen, T. A. Ehlers, N. Insel, Onset of convective rainfall during gradual late Miocene rise of the central Andes. *Science* **328**, 490–493 (2010).
38. J. L. Conroy, D. Noone, K. M. Cobb, J. W. Moerman, B. L. Konecky, Paired stable isotopologues in precipitation and vapor: A case study of the amount effect within western tropical Pacific storms. *J. Geophys. Res. Atmos.* **121**, 3290–3303 (2016).
39. S. Bony, C. Risi, F. Vimeux, Influence of convective processes on the isotopic composition ($\delta^{18}\text{O}$ and δD) of precipitation and water vapor in the tropics: 1. Radiative-convective equilibrium and Tropical Ocean–Global Atmosphere–Coupled Ocean–Atmosphere Response Experiment (TOGA-COARE) simulations. *J. Geophys. Res. Atmos.* **113**, 10.1029/2008JD009942, (2008).
40. L. C. Kanner, S. J. Burns, H. Cheng, R. L. Edwards, High-latitude forcing of the South American summer monsoon during the last glacial. *Science* **335**, 570–573 (2012).
41. V. F. Novello, F. W. Cruz, M. Vuille, N. M. Strikis, R. L. Edwards, H. Cheng, S. Emerick, M. S. De Paula, X. Li, E. de S. Barreto, I. Karmann, R. V. Santos, A high-resolution history of the South American Monsoon from last glacial maximum to the Holocene. *Sci. Rep.* **7**, 44267 (2017).
42. J. Zhu, Z. Liu, E. C. Brady, B. L. Otto-Bliesner, S. A. Marcott, J. Zhang, X. Wang, J. Nusbaumer, T. E. Wong, A. Jahn, D. Noone, Investigating the direct meltwater effect in terrestrial oxygen-isotope paleoclimate records using an isotope-enabled Earth system model. *Geophys. Res. Lett.* **44**, 12501–12510 (2017).
43. J. Worden, K. Bowman, D. Noone, R. Beer, S. Clough, A. Eldering, B. Fisher, A. Goldman, M. Gunson, R. Herman, S. S. Kulawik, M. Lampel, M. Luo, G. Osterman, C. Rinsland, C. Rodgers, S. Sander, M. Shephard, H. Worden, Tropospheric emission spectrometer observations of the tropospheric HDO/H₂O ratio: Estimation approach and characterization. *J. Geophys. Res. Atmos.* **111**, 10.1029/2005JD006606, (2006).
44. J. Worden, S. Kulawik, C. Frankenberg, V. Payne, K. Bowman, K. Cady-Peirara, K. Wecht, J. E. Lee, D. Noone, Profiles of CH₄, HDO, H₂O, and N₂O with improved lower tropospheric vertical resolution from Aura TES radiances. *Atmospheric Meas. Tech.* **5**, 397–411 (2012).
45. C. J. Diekmann, M. Schneider, B. Ertl, F. Hase, O. Garcia, F. Khosravi, E. Sepúlveda, P. Knippertz, P. Braesicke, The global and multi-annual MUSICA IASI (H₂O, δD) pair dataset. *Earth Syst. Sci. Data* **13**, 5273–5292 (2021).
46. S. Sutanto, G. Hoffmann, J. Worden, R. Scheepmaker, I. Aben, T. Roeckmann, Atmospheric processes governing the changes in water isotopologues during ENSO events from model and satellite measurements. *J. Geophys. Res. Atmos.* **120**, 6712–6729 (2015).
47. D. M. Roms, An analytical model for tropical relative humidity. *J. Climate* **27**, 7432–7449 (2014).
48. S. Q. Duan, J. S. Wright, D. M. Roms, On the utility (or futility) of using stable water isotopes to constrain the bulk properties of tropical convection. *J. Adv. Model. Earth Syst.* **10**, 516–529 (2018).
49. Z. Kuang, G. C. Toon, P. O. Wennberg, Y. L. Yung, Measured HDO/H₂O ratios across the tropical tropopause. *Geophys. Res. Lett.* **30**, 10.1029/2003GL017023, (2003).

50. J. Worden, D. Noone, K. Bowman; The Tropospheric Emission Spectrometer science team and data contributors, Importance of rain evaporation and continental convection in the tropical water cycle. *Nature* **445**, 528–532 (2007).
51. J.-E. Lee, I. Fung, “Amount effect” of water isotopes and quantitative analysis of post-condensation processes. *Hydrol. Process.* **22**, 1–8 (2008).
52. C. S. Bretherton, A. H. Sobel, The Gill model and the weak temperature gradient approximation. *J. Atmos. Sci.* **60**, 451–460 (2003).
53. D. Rind, D. Peteet, Terrestrial conditions at the Last Glacial Maximum and CLIMAP sea-surface temperature estimates: Are they consistent? *Quatern. Res.* **24**, 1–22 (1985).
54. A. G. Klein, G. O. Seltzer, B. L. Isacks, Modern and last local glacial maximum snowlines in the Central Andes of Peru, Bolivia, and Northern Chile. *Quat. Sci. Rev.* **18**, 63–84 (1999).
55. S. C. Porter, Snowline depression in the tropics during the Last Glaciation. *Quat. Sci. Rev.* **20**, 1067–1091 (2000).
56. A. M. Seltzer, J. Ng, W. Aeschbach, R. Kipfer, J. T. Kulongoski, J. P. Severinghaus, M. Stute, Widespread six degrees Celsius cooling on land during the Last Glacial Maximum. *Nature* **593**, 228–232 (2021).
57. MARGO Project Members, Constraints on the magnitude and patterns of ocean cooling at the Last Glacial Maximum. *Nat. Geosci.* **2**, 127–132 (2009).
58. J. E. Tierney, J. Zhu, J. King, S. B. Malevich, G. J. Hakim, C. J. Poulsen, Glacial cooling and climate sensitivity revisited. *Nature* **584**, 569–573 (2020).
59. M. B. Osman, J. E. Tierney, J. Zhu, R. Tardif, G. J. Hakim, J. King, C. J. Poulsen, Globally resolved surface temperatures since the Last Glacial Maximum. *Nature* **599**, 239–244 (2021).
60. P. Webster, N. Stretten, Late Quaternary ice age climates of tropical Australasia: Interpretations and reconstructions. *Quatern. Res.* **10**, 279–309 (1978).
61. T. R. Knutson, S. Manabe, Time-mean response over the tropical Pacific to increased CO₂ in a coupled ocean-atmosphere model. *J. Climate* **8**, 2181–2199 (1995).
62. J. D. Shakun, P. U. Clark, F. He, S. A. Marcott, A. C. Mix, Z. Liu, B. Otto-Bliesner, A. Schmittner, E. Bard, Global warming preceded by increasing carbon dioxide concentrations during the last deglaciation. *Nature* **484**, 49–54 (2012).
63. L. G. Thompson, E. Mosley-Thompson, K. A. Henderson, Ice-core palaeoclimate records in tropical South America since the Last Glacial Maximum. *J. Quat. Sci.* **15**, 377–394 (2000).
64. M. Meinshausen, S. Smith, K. Calvin, J. Daniel, M. Kainuma, J. Lamarque, K. Matsumoto, S. Montzka, S. Raper, K. Riahi, The paleoclimate modeling intercomparison project contribution to CMIP5. *WCRP Coupled Model Intercomp. Proj.-Phase 5-CMIP5*. **16**, 15–51 (2011).
65. M. Kageyama, P. Braconnot, S. P. Harrison, A. M. Haywood, J. H. Jungclaus, B. L. Otto-Bliesner, J.-Y. Peterschmitt, A. Abe-Ouchi, S. Albani, P. J. Bartlein, The PMIP4 contribution to CMIP6—Part 1: Overview and over-arching analysis plan. *Geosci. Model Dev.* **11**, 1033–1057 (2018).
66. E. Brady, S. Stevenson, D. Bailey, Z. Liu, D. Noone, J. Nusbaumer, B. Otto-Bliesner, C. Tabor, R. Tomas, T. Wong, J. Zhang, J. Zhu, The connected isotopic water cycle in the Community Earth System Model version 1. *J. Adv. Model. Earth Syst.* **11**, 2547–2566 (2019).
67. T. S. von Deimling, A. Ganopolski, H. Held, S. Rahmstorf, How cold was the Last Glacial Maximum? *Geophys. Res. Lett.* **33**, L14709 (2006).
68. P. B. Holden, N. Edwards, K. Oliver, T. Lenton, R. Wilkinson, A probabilistic calibration of climate sensitivity and terrestrial carbon change in GENIE-1. *Clim. Dynam.* **35**, 785–806 (2010).
69. A. Schmittner, N. M. Urban, J. D. Shakun, N. M. Mahowald, P. U. Clark, P. J. Bartlein, A. C. Mix, A. Rosell-Melé, Climate sensitivity estimated from temperature reconstructions of the Last Glacial Maximum. *Science* **334**, 1385–1388 (2011).
70. J. D. Annan, J. C. Hargreaves, A new global reconstruction of temperature changes at the Last Glacial Maximum. *Clim. Past* **9**, 367–376 (2013).
71. C. W. Snyder, Evolution of global temperature over the past two million years. *Nature* **538**, 226–228 (2016).
72. B. Bereiter, S. Shackleton, D. Baggenstos, K. Kawamura, J. Severinghaus, Mean global ocean temperatures during the last glacial transition. *Nature* **553**, 39–44 (2018).
73. T. Friedrich, A. Timmermann, Using Late Pleistocene sea surface temperature reconstructions to constrain future greenhouse warming. *Earth Planet. Sci. Lett.* **530**, 115911 (2020).
74. J. D. Annan, J. C. Hargreaves, T. Mauritsen, A new global surface temperature reconstruction for the Last Glacial Maximum. *Clim. Past* **18**, 1883–1896 (2022).
75. C. He, Z. Liu, B. L. Otto-Bliesner, E. C. Brady, C. Zhu, R. Tomas, C. Buizert, J. P. Severinghaus, Abrupt Heinrich Stadial 1 cooling missing in Greenland oxygen isotopes. *Sci. Adv.* **7**, eab11007 (2021).
76. Z. Liu, C. He, M. Yan, C. Buizert, B. Otto-Bliesner, F. Lu, C. Zeng, Reconstruction of past Antarctic temperature using present seasonal $\delta^{18}O$ -inversion layer temperature: Unified slope equations and applications. *J. Climate* **36**, 2933–2957 (2023).
77. D. M. Roms, Rayleigh damping in the free troposphere. *J. Atmos. Sci.* **71**, 553–565 (2014).
78. C. M. Bender, S. Orszag, S. A. Orszag, *Advanced Mathematical Methods for Scientists and Engineers I: Asymptotic Methods and Perturbation Theory* (Springer Science & Business Media, 1999), 1.
79. D. Noone, Pairing measurements of the water vapor isotope ratio with humidity to deduce atmospheric moistening and dehydration in the tropical midtroposphere. *J. Climate* **25**, 4476–4494 (2012).
80. E. J. Moyer, F. W. Irion, Y. L. Yung, M. R. Gunson, ATMOS stratospheric deuterated water and implications for troposphere-stratosphere transport. *Geophys. Res. Lett.* **23**, 2385–2388 (1996).
81. G. J. Zhang, X. Wu, X. Zeng, T. Mitovski, Estimation of convective entrainment properties from a cloud-resolving model simulation during TWP-ICE. *Clim. Dynam.* **47**, 2177–2192 (2016).
82. W. C. De Rooy, P. Bechtold, K. Fröhlich, C. Hohenegger, H. Jonker, D. Mironov, A. Pier Siebesma, J. Teixeira, J.-I. Yano, Entrainment and detrainment in cumulus convection: An overview. *Q. J. Roy. Meteorol. Soc.* **139**, 1–19 (2013).
83. S. Botsyun, P. Sepulchre, Y. Donnadieu, C. Risi, A. Licht, J. K. Caves Rugenstein, Revised paleoaltimetry data show low Tibetan Plateau elevation during the Eocene. *Science* **363**, eaq1436 (2019).
84. A. Rohrmann, M. R. Strecker, B. Bookhagen, A. Mulch, D. Sachse, H. Pingel, R. N. Alonso, T. F. Schildgen, C. Montero, Can stable isotopes ride out the storms? The role of convection for water isotopes in models, records, and paleoaltimetry studies in the central Andes. *Earth Planet. Sci. Lett.* **407**, 187–195 (2014).
85. Z. Jing, W. Yu, S. Lewis, L. G. Thompson, J. Xu, J. Zhang, B. Xu, G. Wu, Y. Ma, Y. Wang, R. Guo, Inverse altitude effect disputes the theoretical foundation of stable isotope paleoaltimetry. *Nat. Commun.* **13**, 4371 (2022).
86. P. Keil, H. Schmidt, B. Stevens, J. Bao, Variations of tropical lapse rates in climate models and their implications for upper-tropospheric warming. *J. Climate* **34**, 9747–9761 (2021).
87. O. Miyawaki, Z. Tan, T. A. Shaw, M. F. Jansen, Quantifying key mechanisms that contribute to the deviation of the tropical warming profile from a moist adiabat. *Geophys. Res. Lett.* **47**, e2020GL089136 (2020).
88. P. Grootes, M. Stuiver, L. Thompson, E. Mosley-Thompson, Oxygen isotope changes in tropical ice, Quelccaya, Peru. *J. Geophys. Res. Atmos.* **94**, 1187–1194 (1989).
89. W. Stichler, U. Schotterer, K. Fröhlich, P. Ginot, C. Kull, H. Gäggeler, B. Pouyaud, Influence of sublimation on stable isotope records recovered from high-altitude glaciers in the tropical Andes. *J. Geophys. Res. Atmos.* **106**, 22613–22620 (2001).
90. K. Rozanski, L. Araguás Araguás, Spatial and temporal variability of stable isotope composition of precipitation over the South American continent. *Bull. Inst. Fr. Etudes Andin.* **24**, 379–390 (1995).
91. J. Jouzel, L. Merlivat, Deuterium and oxygen 18 in precipitation: Modeling of the isotopic effects during snow formation. *J. Geophys. Res. Atmos.* **89**, 11749–11757 (1984).
92. M. Cai, Dynamical amplification of polar warming. *Geophys. Res. Lett.* **32**, 10.1029/2005GL024481, (2005).
93. V. Masson-Delmotte, M. Kageyama, P. Braconnot, S. Charbit, G. Krinner, C. Ritz, E. Guilyardi, J. Jouzel, A. Abe-Ouchi, M. Crucifix, R. M. Gladstone, C. D. Hewitt, A. Kitoh, A. N. LeGrande, O. Marti, U. Merkel, T. Motoi, R. Ohgaito, B. Otto-Bliesner, W. R. Peltier, I. Ross, P. J. Valdes, G. Vettoretti, S. L. Weber, F. Wolk, Y. Yu, Past and future polar amplification of climate change: Climate model intercomparisons and ice-core constraints. *Clim. Dynam.* **26**, 513–529 (2006).

Acknowledgments: We thank D. Noone, J. Zhu, J. Shakun, and P. Clark for helpful discussions. **Funding:** This study was supported by NSF AGS2002506, AGS2002521 (Z.L., Y.B., L.G.T., and E. M.-T.), LSKJ202203300 (Y.B.), NSF AGS1804747, AGS1754998, AGS180426 (C.T., M.L., I.M., and J. O.), and AGS2054697 (G.J.Z.). The 2019 Huascarán ice core drilling and analyses were supported by NSF AGS1805819 and the 1993 Huascarán and 1997 Sajama drilling and analyses were funded by awards from NOAA and NSF (L.G.T. and E.M.-T.). **Author contributions:** Z.L. and Y.B. conceived the study. Z.L. wrote the paper. Y.B. performed the analysis. Z.L. and G.J.Z. contributed to the theory. L.G.T. and E.M.-T. contributed to paleo proxy studies and interpretations. C.T., M.L., I.M., and J.O. contributed to the HighRes simulation. Y.B. and MY performed the PMIP analysis. All authors contributed to the discussions and the manuscript. **Competing interests:** The authors declare that they have no competing interests. **Data and materials availability:** All data needed to evaluate the conclusions in the paper are present in the paper and/or the Supplementary Materials. Paleoclimate ice core data can be found from NOAA (<https://ncdc.noaa.gov/data-access/paleoclimatology-data>). The present-day water isotope observation data (GNIP) can be found from the International Atomic Energy Agency (<https://iaea.org/services/networks/gnip>). The TES version 6, level 3 monthly water vapor, deuterium oxide, and atmospheric temperature data, covering the period 2004 to 2012, is available from NASA's Atmospheric Science Data Center: <https://earthdata.nasa.gov/eosdis/daacs/asdc>. The posteriori processed MUSICA IASI daily regridded level 3 water vapor and deuterium oxide dataset, covering 2014 to 2020, is available from Karlsruhe Institute of Technology: <https://radar.kit.edu/radar/en/dataset/elgWmcoTbouvnm#>. The PMIP3 and

PMIP4 (Palaeoclimate Modelling Intercomparison Project Phase III & IV) model data for LGM and PI control simulations can be downloaded from <https://esgf-node.llnl.gov/search/cmip5/> and <https://esgf-node.llnl.gov/search/cmip6/>, respectively. PMIP2 model data can be found at <https://pmip2.lsce.ipsl.fr/>. All iTRACE simulation data used in this study can be found at <https://earthsystemgrid.org/dataset/ucar.cgd.cesm4.iTRACE.html>. The data necessary to reproduce main text figures and postprocessed data for analysis are available at <https://zenodo.org/record/8171476>. iCESM is freely available as open-source code from <https://github.com/NCAR/>

iCESM1.2. All analysis, calculations, and plots were carried out using Python 3.9. The codes for generating the main text figures are available at <https://zenodo.org/record/8171476>.

Submitted 10 May 2023

Accepted 12 October 2023

Published 8 November 2023

10.1126/sciadv.adi6725